# Reprocessed, Bias-Corrected CMORPH Global High-Resolution Precipitation Estimates from 1998

PINGPING XIE

*NOAA/Climate Prediction Center, College Park, Maryland*

ROBERT JOYCE AND SHAORONG WU

*NOAA/Climate Prediction Center, College Park, and Innovim, LLC, Greenbelt, Maryland*

SOO-HYUN YOO AND YELENA YAROSH

*NOAA/Climate Prediction Center, College Park, Maryland, and Wyle, Inc., McLean, Virginia*

FENGYING SUN AND ROGER LIN

*NOAA/Climate Prediction Center, College Park, and Innovim, LLC, Greenbelt, Maryland*

(Manuscript received 14 July 2016, in final form 22 November 2016)

ABSTRACT

The Climate Prediction Center (CPC) morphing technique (CMORPH) satellite precipitation estimates are reprocessed and bias corrected on an 8 km × 8 km grid over the globe (60°S–60°N) and in a 30-min temporal resolution for an 18-yr period from January 1998 to the present to form a climate data record (CDR) of high-resolution global precipitation analysis. First, the purely satellite-based CMORPH precipitation estimates (raw CMORPH) are reprocessed. The integration algorithm is fixed and the input level 2 passive microwave (PMW) retrievals of instantaneous precipitation rates are from identical versions throughout the entire data period. Bias correction is then performed for the raw CMORPH through probability density function (PDF) matching against the CPC daily gauge analysis over land and through adjustment against the Global Precipitation Climatology Project (GPCP) pentad merged analysis of precipitation over ocean. The reprocessed, bias-corrected CMORPH exhibits improved performance in representing the magnitude, spatial distribution patterns, and temporal variations of precipitation over the global domain from 60°S to 60°N. Bias in the CMORPH satellite precipitation estimates is almost completely removed over land during warm seasons (May–September), while during cold seasons (October–April) CMORPH tends to underestimate the precipitation due to the less-than-desirable performance of the current-generation PMW retrievals in detecting and quantifying snowfall and cold season rainfall. An intercomparison study indicated that the reprocessed, bias-corrected CMORPH exhibits consistently superior performance than the widely used TRMM 3B42 (TMPA) in representing both daily and 3-hourly precipitation over the contiguous United States and other global regions.

## 1. Introduction

One great achievement of the recent three decades in the area of geosciences is the construction of global precipitation products with refined resolution and improved quality. Virtually the only quantitative global precipitation datasets available in the early 1990s were the estimated monthly climatology fields at a 2.5° latitude–longitude (lat–lon) grid (Jaeger 1976; Legates and Willmott 1990). Now observation-based precipitation analyses are routinely produced on a fine time (space) resolution of 30 min (8 km × 8 km) over a quasi-global domain. Particularly noticeable is the development of satellite-based, high-resolution, long-term precipitation analyses.

At least six such datasets have been developed in recent years to facilitate improved research and applications in meteorology, hydrometeorology, and hydrology. Pioneering the efforts in this front, Hsu et al. (1997) developed a sophisticated system to convert geostationary (GEO) satellite infrared (IR) blackbody temperatures (TBB) into instantaneous rain rate through an

*Corresponding author e-mail*: Pingping Xie, pingping.xie@noaa.gov

DOI: 10.1175/JHM-D-16-0168.1

artificial neural network. A regionally dependent and temporally evolving TBB–precipitation relationship is established by training concurrent GEO IR data against precipitation estimates derived from passive microwave (PMW) channel measurements from low-Earth-orbiting (LEO) platforms with a neural network system. This technique, called Precipitation Estimation from Remotely Sensed Information Using Artificial Neural Network (PERSIANN), is further improved by including additional information on cloud type information (Hong et al. 2007). A climate data record (CDR) of the PERSIANN daily precipitation is created through reprocessing the raw estimates for an extended period from 1981 to the present and calibrating the reprocessed satellite precipitation estimates against the Global Precipitation Climatology Project (GPCP) merged analysis of monthly precipitation (Ashouri et al. 2015).

Turk et al. (2003, 2010) and Huffman et al. (2007) developed algorithms that produce IR-based precipitation estimates by matching the probability density function (PDF) of GEO IR TBB with collocated LEO PMW-derived precipitation intensity and then combining these IR-based estimates with PMW data to produce precipitation maps of fine spatial–temporal resolution. The algorithm of Turk et al. (2003) has been implemented at the Naval Research Laboratory (NRL) to generate high-resolution global precipitation estimates on a real-time basis since 2004. The technique of Huffman et al. (2007), called Tropical Rainfall Measuring Mission (TRMM) Multisatellite Precipitation Analysis (TMPA), is adopted by the TRMM program to generate level 3 gridded precipitation products, TRMM 3B42 and its real-time version 3B42RT. TRMM 3B42RT is postprocessed with all available inputs and calibrated against the Global Precipitation Climatology Centre (GPCC) monthly gauge analysis over land (Becker et al. 2013; Schneider et al. 2014) to remove biases in the satellite estimates (Huffman and Bolvin 2014). The TMPA data are generated on a 0.25° lat–lon grid over the globe (50°S–50°N) and at a 3-hourly temporal resolution from 1998 to the present.

The CPC morphing technique (CMORPH; Joyce et al. 2004), meanwhile, takes a very different approach to take advantage of the high temporal resolution of the GEO IR observations. Motion vectors of the cloud systems are first defined from the consecutive GEO IR images through the cross-correlation technique. Precipitation analyses are then produced at 30-min intervals and on an 8 km × 8 km grid over the globe through the propagation of precipitating cloud clusters observed by the instantaneous PMW estimates along cloud motion vectors. A similar Lagrangian approach is adopted by Ushio et al. (2009), who developed a Kalman filtering–based method to construct maps of hourly precipitation on a 0.1° lat–lon grid over the globe.

Latest in the development in this area is the IMERG high-resolution satellite precipitation estimates as the United States' official Global Precipitation Measurement (GPM) mission (Hou et al. 2010) level 3 precipitation product (Huffman et al. 2011). The integration framework of the IMERG technique is based on the Kalman filter version CMORPH (Joyce and Xie 2011), combined with the intercalibration and bias-adjustment algorithms from TMPA (Huffman et al. 2007) and the GEO IR estimation method adopted from PERSIANN (Hsu et al. 1997). Starting in March 2014, the IMERG 30-min precipitation estimates are produced on a quasi-real-time basis on a 0.1° lat–lon grid from 60°S to 60°N.

Evaluation studies have shown improved performance of these satellite integration techniques in constructing precipitation analyses upon individual PMW-based retrievals, especially over tropical and subtropical areas (Ebert et al. 2007). The high-resolution precipitation estimates created by these algorithms enabled a variety of applications in weather, climate, and hydrology, including the examination of diurnal cycle of precipitation over the globe, forcing land surface models, and real-time global flooding monitoring (e.g., Cosgrove et al. 2003; Xie et al. 2012; Wu et al. 2012; Meng et al. 2012).

Among the high-resolution global precipitation datasets mentioned above, CMORPH presents superior performance in capturing the spatial distribution and temporal variations over most of the global regions as verified by relatively high correlations with independent surface observation data in numerous validation studies (e.g., Xie et al. 2007; Sapiano and Arkin 2009). Discontinuities, however, are observed in the time series of the operational CMORPH satellite precipitation estimates (hereafter referred to as version 0.X). Many changes have occurred to the CMORPH integration algorithm and the input level 2 satellite retrievals since the commencement of the operational production of the CMORPH version 0.X in December 2002. Another shortcoming of the CMORPH version 0.X is the existence of biases in the integrated satellite precipitation estimates passed through from the input PMW retrievals (Sapiano and Arkin 2009; Habib et al. 2012). Changing with region, season, surface type, diurnal cycle, and precipitation intensity, these biases compromise quantitative applications of the dataset, especially in hydrology, hydrometeorology, and air–sea interaction studies (Tian et al. 2009; Xu et al. 2010; Wu et al. 2012; Tang et al. 2014).

Two objectives of this work are 1) to reprocess the CMORPH satellite precipitation estimates for the entire TRMM/GPM era from 1998 to the present using a

TABLE 1. PMW sensors whose measurements are used to derive level 2 precipitation retrievals.

| PMW sensor | LEO platform carrying the sensor |
|---|---|
| TMI | TRMM |
| Advanced Microwave Scanning Radiometer (AMSR) | *Aqua* |
| Special Sensor Microwave Imager/Sounder (SSMIS) | Defense Meteorological Satellite Program (DMSP) *F-16*, *F-17*, and *F-18* |
| Special Sensor Microwave Imager (SSM/I) | DMSP *F-13*, *F-14*, and *F-15* |
| Microwave Humidity Sounder (MHS) | *NOAA-18*, *NOAA-19*, *MetOp-A*, and *MetOp-B* |
| Advanced Microwave Sounding Unit (AMSU) | *NOAA-15*, *NOAA-16,* and *NOAA-17* |
| Microwave Radiation Imager (MWRI) | *Fengyun-3B (FY-3B)* |

fixed version of the integration algorithm and with input PMW retrievals of identical versions throughout the data period and 2) to perform bias correction for the raw integrated CMORPH satellite precipitation estimates through comparison with gauge data over land and calibration against the GPCP merged analysis over ocean. The result of the work is a homogenous CDR of high-resolution (30 min and 8 km × 8 km) global precipitation for an extended period from January 1998 to the present. Sections 2 and 3 provide detailed descriptions of the CMORPH reprocessing and bias correction procedures, respectively. Section 4 presents an examination of the reprocessed, bias-corrected CMORPH against ground observations and an intercomparison with a similar product (TMPA, version 7/TRMM 3B42). A summary will be given in section 5.

## 2. The CMORPH algorithm, input data, and reprocessing

One important requirement for a CDR of satellite-based, long-term time series of essential climate variables is the temporal and spatial homogeneity (Bates and Barkstrom 2006). To satisfy this requirement, the CMORPH high-resolution global precipitation estimates are reprocessed using a fixed version of the integration algorithm and with input PMW retrievals of identical versions throughout the data period.

### *a. Input satellite data*

The purely satellite-based CMORPH precipitation estimates (the raw CMORPH) are created with inputs from three categories of spaceborne measurements as detailed below.

#### 1) LEVEL 2 PMW RETRIEVALS OF PRECIPITATION RATE

Level 2 retrievals from PMW sensors aboard multiple LEO satellites are used in this work to construct the CMORPH integrated satellite estimates. Table 1 lists satellite PMW sensors whose measurements are used to derive the level 2 precipitation retrievals served as inputs to the raw CMORPH. Over ocean, retrievals of precipitation are derived from PMW emission and scattering channels taking advantage of the relationship between surface precipitation and the vertical profile of liquid water. Over land, scattering channels are used assuming that concentration of frozen hydrometeors and large water droplets inside the clouds are associated with the precipitation rate at surface. The input level 2 PMW retrievals derived from PMW imagers are generated using the GPROF, version 2004, algorithms (Kummerow et al. 2001). Precipitation retrievals from PMW sounders are produced using the Microwave Surface and Precipitation Products System (MSPPS; Ferraro et al. 2005).

#### 2) SATELLITE-BASED SNOW/ICE MAPS

Interactive Multisensor Snow and Ice Mapping System (IMS) daily 4-km snow and sea ice cover maps over the Northern Hemisphere are used in this work to mask out areas where PMW retrievals of precipitation may be contaminated by the noise from the snow/ice over the ground. The IMS snow/ice maps are constructed by combining information from a variety of sources, including the in situ measurements and satellite images of visible and PMW channels (Armstrong and Brodzik 2002; Helfrich et al. 2007). This dataset is created by NOAA/National Environmental Satellite, Data, and Information Service (NESDIS) under the direction of the NOAA Ice Center (NIC) and updated on a quasi-real-time basis. No similar snow/ice maps are available for the Southern Hemisphere for the entire data period of our CMORPH reprocessing.

#### 3) FULL-RESOLUTION GEO IR DATA

Full-resolution global surface/cloud-top temperature data of Janowiak et al. (2001) are used to derive cloud motion vectors as part of the CMORPH processing. The global array of IR TBB is constructed at NOAA/CPC through compositing IR window channel measurements from five geostationary satellites located above the equator at the Atlantic Ocean, Africa, the Indian Ocean, the western Pacific Ocean, and the eastern

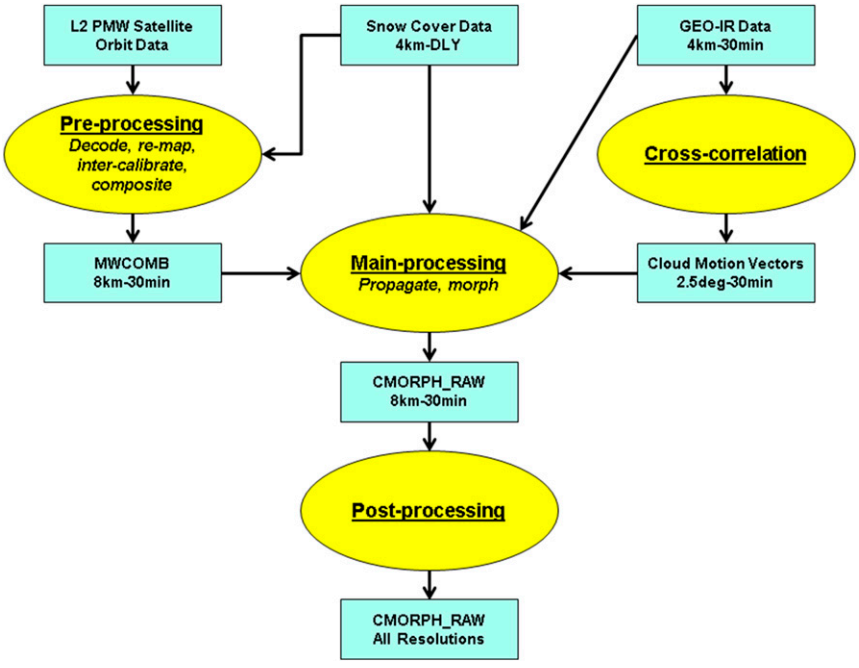


FIG. 1. Flowchart of the raw CMORPH integrated satellite precipitation estimates.

Pacific Ocean. The full-resolution IR data are produced on a 4 km × 4 km grid over the global domain (60°S–60°N) and in a 30-min interval starting on 1 January 1998.

### b. *The CMORPH integration algorithm*

#### 1) PREPROCESSING

The raw CMORPH is constructed through integrating precipitation information from multiple PMW sensors aboard LEO satellites (Fig. 1). Preprocessing is first performed for the level 2 precipitation rate retrievals from all available PMW sensors (Fig. 1, left). Level 2 retrievals at respective satellite footprints are remapped to a common equal angle global grid system of 8 km × 8 km at the equator. Calibration is then performed through PDF matching against a common reference field using temporally–spatially collocated data pairs. Precipitation retrievals from the TRMM/TRMM Microwave Imager (TMI) are utilized as the calibrator here for their high quality and the availability of temporally–spatially coincident matching samples with all other PMW sensors. These coincident samples are made possible by the precessing orbit pattern of the TRMM satellite (Simpson et al. 1988). Updated once a month, this PDF calibration table is constructed for each 10° latitude band and for land and ocean separately using collocated data pairs available over the target month. This calibration ensures input PMW retrievals from individual sensors present close PDF characteristics.

Because of the loss of TMI measurements in April 2015, the PDF tables used to perform intercalibration of PMW level 2 precipitation rate retrievals as described above can no longer be updated. To continue the intercalibration for PMW retrievals after April 2015, a set of PDF tables are established for PMW retrievals from each sensor using historical data. The climatological PDF tables are constructed for each calendar month to account for seasonal variations, for every 10° latitude band to reflect regional differences, and for land and ocean separately.

#### 2) COMPOSITING

The remapped and calibrated level 2 PMW precipitation rate retrievals are then composited into a single global field of precipitation estimates, called MWCOMB, at a time (space) resolution of 30 min (8 km × 8 km). When PMW retrievals from multiple sensors are available over a specific grid box and for a specific 30-min time slot, only the one with the highest quality is used to define the MWCOMB. The quality of PMW retrievals from various sensors is ranked, as shown in Table 2. This ranking is based on published studies by other scientists (e.g., Tian et al. 2009) as well as our own examinations (e.g., Joyce and Xie 2011). Every time a new version of level 2 precipitation retrievals is available from a new or existing sensor, a set of examination procedures is implemented by the

TABLE 2. Quality ranking of PMW precipitation retrievals from various sensors aboard various platforms.

| Quality ranking | PMW sensor (decreasing quality from top to bottom) | LEO platforms (decreasing quality from left to right) |
|---|---|---|
| 1 | TMI | TRMM |
| 2 | AMSR | *Aqua* |
| 3 | MWRI | *FY-3B* |
| 4 | SSMIS | *F-18*, *F-17*, and *F-16* |
| 5 | SSM/I | *F-15*, *F-14*, and *F-13* |
| 6 | MHS | *MetOp-B*, *MetOp-A*, *NOAA-19*, and *NOAA-18* |
| 7 | AMSU | *NOAA-17*, *NOAA-16*, and *NOAA-15* |

CMORPH developers at CPC to quantify the error of the level 2 products through comparison against surface radar estimates and gauge observations. As shown in Table 2, PMW imager-equipped satellites consistently yield higher rankings than PMW sounder satellites.

Quality control is performed for the MWCOMB to eliminate erroneous and suspicious PMW retrievals over grid boxes of 8 km × 8 km where the IMS daily snow cover maps indicate any contamination of snow or ice. Figure 2a illustrates an example of the MWCOMB for the 30-min window starting at 0000 UTC 1 August 2014. While the PMW retrievals are capable of depicting distribution patterns of instantaneous precipitation quite well, only a small portion of the global domain is covered by the PMW orbits for the 30-min window even with as many as eight LEO satellites.

### 3) CLOUD MOTION VECTORS

In the meantime, cloud motion vectors are computed from consecutive GEO IR images in 30-min intervals (Janowiak et al. 2001) through the cross-correlation technique (Fig. 1, right). The cross-correlation technique has been long used for automatic tracking of cloud motion (Leese et al. 1971). Cloud motion vectors are calculated for each grid box of 2.5° lat–lon using data

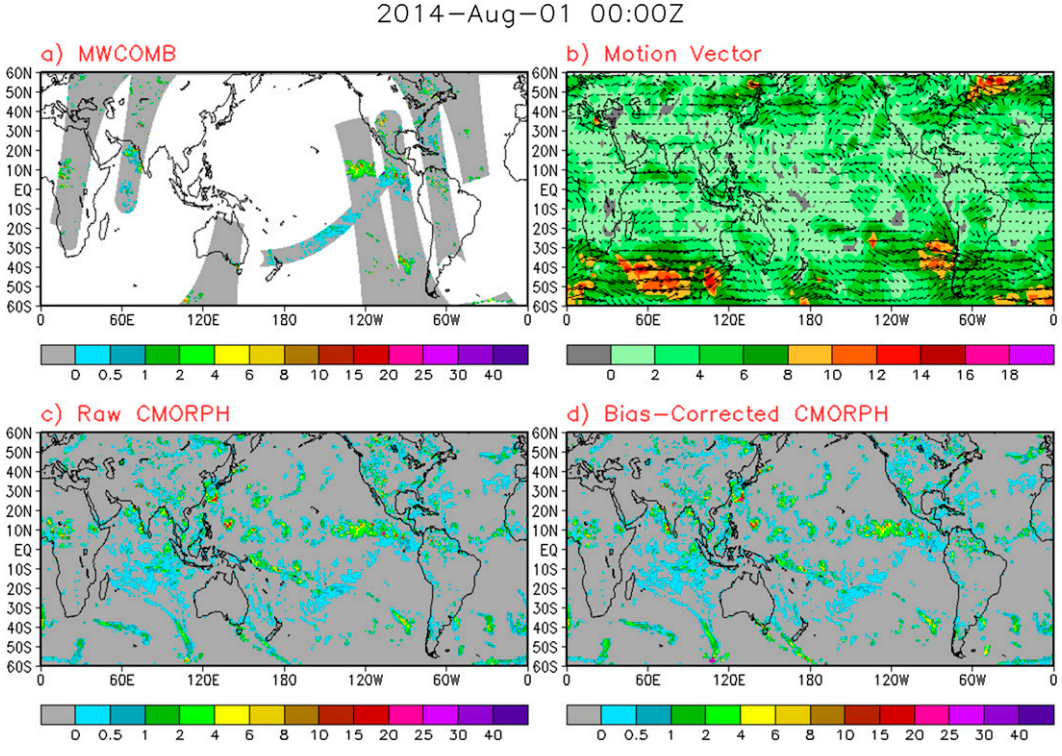


FIG. 2. Samples of global fields of (a) composite calibrated PMW precipitation retrievals (MWCOMB; mm $h^{-1}$), (b) cloud motion vector, (c) raw CMORPH (mm $h^{-1}$), and (d) bias-corrected CMORPH (mm $h^{-1}$), for the 30-min time slot beginning at 0000 UTC 1 Aug 2014. In (b), arrows indicate the direction while the color shading represents the speed (in number of 8 km × 8 km grid boxes).

over a 5° lat–lon domain centering at the target grid box. Spatial pattern correlation is computed between the GEO IR TBB data array for the target analysis time and that for the previous time step at a combination of spatial displacements in both zonal and meridional directions. The spatial displacement with the maximum correlation is assumed to be caused by the mean movement of the cloud systems over the region and is used to define the cloud motion vector at the target grid point. The cloud motion vectors are adjusted through comparisons with precipitation propagation derived from radar precipitation. The cloud motion vector defined on the 2.5° lat–lon grid system is then downscaled to the MWCOMB resolution of 8 km × 8 km through bilinear interpolation. Figure 2b shows an example of the cloud motion vectors at 0000 UTC 1 August 2014. Cloud movements associated with the synoptic weather systems over both hemispheres are well captured by our vectors.

#### 4) PROPAGATING AND MORPHING

The PMW precipitation rate retrievals composited in the MWCOMB are then propagated from their respective observation times to the target analysis time (Fig. 1, center). The propagation is conducted in both the forward and backward directions to fully take advantage of the PMW observations at, before, and after the target analysis time. The raw CMORPH integrated satellite precipitation estimation at a grid box of 8 km × 8 km is defined as the weighted mean of the PMW retrievals propagated there from the forward and backward directions with the weights inversely proportional to the temporal length of the propagation.

After the MWCOMB PMW retrievals are propagated and morphed onto an 8 km × 8 km grid and at a 30-min time step, quality control is performed, once again, using the IMS daily surface snow/ice map of NESDIS and the full-resolution IR data of Janowiak et al. (2001) to screen out suspicious precipitation estimates over grid boxes of clear sky or with snow or sea ice coverage (Fig. 1, top center). In the current version of the algorithm, no further steps are taken to fill in the gaps left by the screening process, resulting in incomplete spatial coverage especially during cold seasons. An IR-based technology is under development as part of the next-generation CMORPH to provide reasonable precipitation estimates for those situations (Xie et al. 2016).

#### 5) POSTPROCESSING

Postprocessing (Fig. 1, bottom center) is finally implemented to create global fields of the raw CMORPH precipitation estimates at an assortment of time (space) resolutions, including 30-min (8 km × 8 km), hourly (0.25° lat–lon), daily from 0000 to 0000 UTC (0.25° lat–lon), and daily from the gauge at the end of day (0.25° lat–lon). Figure 2c shows an example of the raw CMORPH at 0000 UTC 1 August 2014. Propagating and morphing the level 2 precipitation retrievals from individual PMW sensors, CMORPH is capable of producing precipitation estimates on a very high time (space) resolution [30 min (8 km × 8 km)] over the globe from 60°S to 60°N.

### c. *Reprocessing of the purely satellite-based CMORPH*

As mentioned in section 1, the CMORPH satellite precipitation estimates have been generated on a real-time basis since December 2002 with an evolving integration algorithm and inputs of varying versions. As the first step of this work, the raw CMORPH estimates have been extended backward in time from the December 2002 operational initiation to January 1998 and reprocessed from January 2003 to the present using the most recent PMW precipitation retrieval algorithm version from all available low-Earth orbiters and IR observations from geostationary platforms.

The input level 2 PMW retrievals of instantaneous precipitation rates are those generated using GPROF, version 2004 (Kummerow et al. 2001). Level 2 data coverages for the PMW sensors aboard various platforms are shown in Fig. 3. While PMW-based precipitation retrievals are available only from three LEO platforms over the first 2 years of the data period, the number of satellites with PMW sensors increases with time, reaching ~10 for most of the period after 2007. The version of the integration algorithm is the implementation code operational as of 2009. Joyce et al. (2004) provide a description of an earlier implementation of the CMORPH algorithm.

The back-extended and reprocessed CMORPH precipitation estimates (the raw CMORPH) consist of a homogeneous record of high-resolution precipitation on an 8 km × 8 km grid covering the globe from 60°S to 60°N and in a 30-min interval covering an 18-yr period from 1998 to the present.

## 3. CMORPH bias correction

Integrated satellite precipitation estimates, such as the raw CMORPH, contain bias passed through from the input level 2 PMW retrievals (Ebert et al. 2007; Tian et al. 2009). Bias correction needs to be performed to ensure improved quantitative accuracy. Among the six sets of integrated satellite precipitation estimates

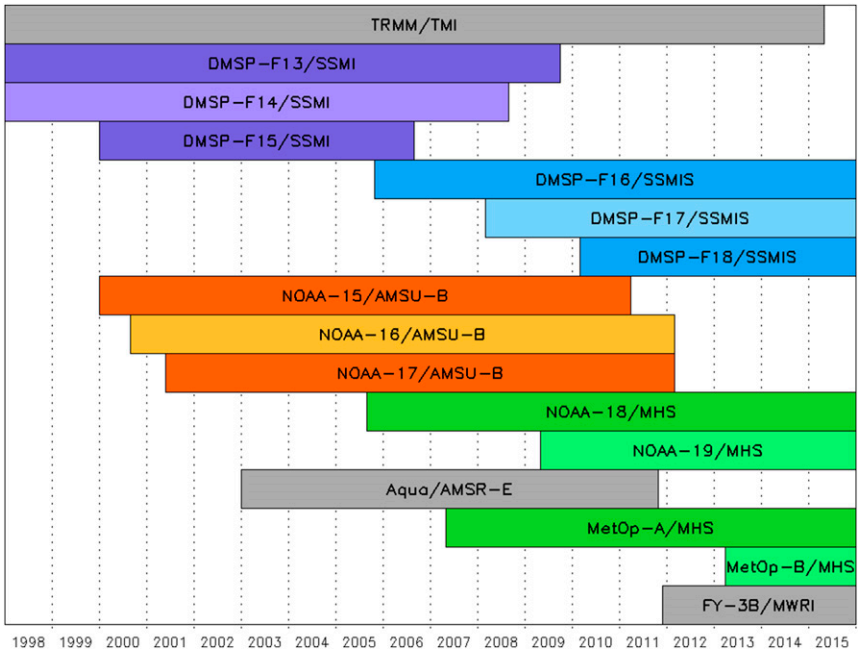


FIG. 3. Availability of level 2 precipitation retrievals derived from measurements of PMW sensors aboard various LEO satellites from January 1998 to December 2015.

discussed in section 1, the TMPA is the first to include the bias correction procedures. The PMW–IR merged precipitation estimates in the TMPA are calibrated against the GPCC monthly gauge analysis (Becker et al. 2013; Schneider et al. 2014) over land and against the TMI–Precipitation Radar (PR) combined precipitation product (TRMM 3B31; Haddad et al. 1997) over the ocean. This bias correction is adopted by IMERG in creating GPM official level 3 gridded precipitation products (Huffman et al. 2011). In constructing the PERSIANN CDR, the purely satellite-based precipitation estimates are adjusted to the GPCP merged analysis of monthly precipitation (Adler et al. 2003) over both land and ocean (Ashouri et al. 2015). In both the TMPA and PERSIANN approaches, the ratio of correction is calculated month by month, leaving the possibility of discontinuities around the monthly boundaries. Recently, the GSMaP team added a new component to their global precipitation product suite by correcting the satellite-based hourly estimates [Global Satellite Mapping of Precipitation moving vector with Kalman filter (GSMaP_MVK)] so that its 24-hourly total matches with the CPC daily gauge analysis (Ushio et al. 2013; Mega et al. 2014).

In this part of the paper, we develop a set of procedures to remove (reduce) the biases in the raw CMORPH precipitation estimates. Because of the differences in both the characteristics of the CMORPH biases and the availability of "ground truth" (reference) datasets, bias correction algorithms are developed separately for land and ocean.

### *a. CMORPH bias correction over land*

#### 1) RAW CMORPH BIAS OVER LAND

While many studies have been conducted to investigate the performance of CMORPH and other high-resolution satellite precipitation estimates in lieu of their capacities in various applications (e.g., Tian et al. 2009; Yong et al. 2012), the objective of this part of our study is to understand the CMORPH error structure for the design and development of an effective bias-removal procedure. Toward this goal, we examine the regional, seasonal dependence, time–space scales, and nonlinearity of the raw CMORPH bias.

CPC gauge-based analysis of daily precipitation (Xie et al. 2010) is used here as the ground truth to quantify the error structures of the CMORPH satellite estimates and, later on, utilized as the reference field in removing the biases in the raw CMORPH over land. Although reports of gauge measurements suffer from wind-induced undercatch, especially for snowfall (Sevruk 1982), and the gauge station network is not appropriate over many sparsely populated and/or mountainous regions (Xie et al. 2010), gauge-based analysis of precipitation exhibits much higher quality than satellite estimates over regions of reasonable station coverage (Xie et al. 2007). Xie and Xiong (2011) investigated the quantitative accuracy of the CPC

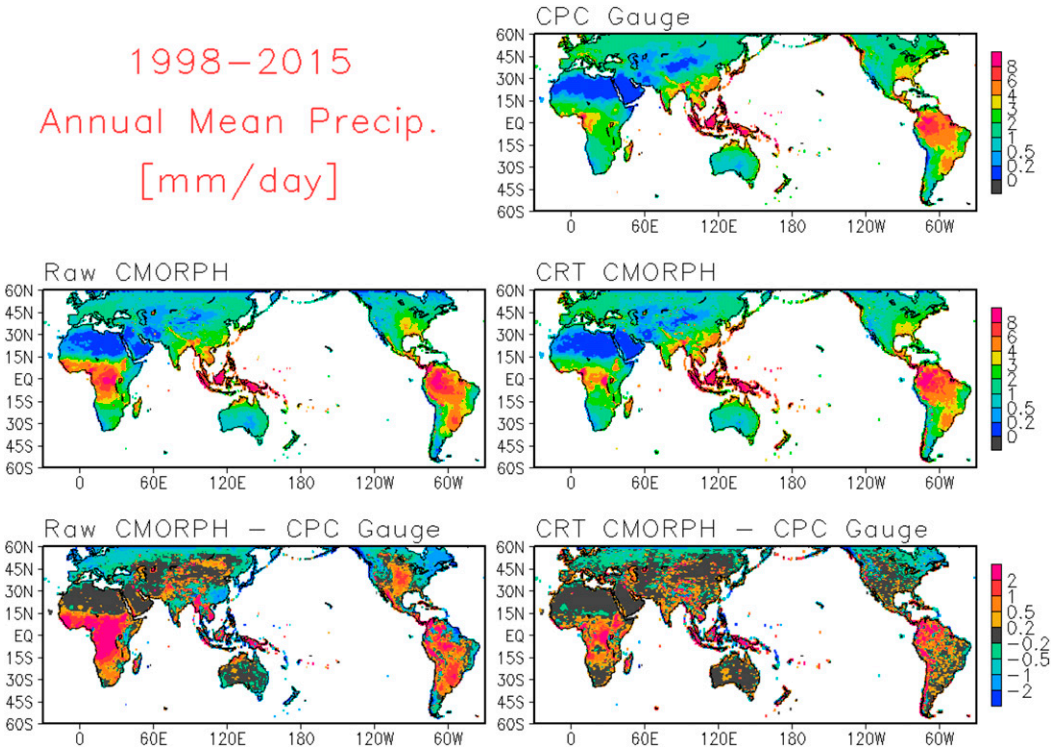


FIG. 4. The 1998–2015 annual mean precipitation (mm day$^{-1}$) for the (top right) CPC Unified gauge analysis of daily precipitation, (middle left) the raw CMORPH, (middle right) the bias-corrected CMORPH, (bottom left) the differences between the raw CMORPH and the CPC gauge, and (bottom right) the differences between the bias-corrected CMORPH and the CPC gauge.

gauge-based analysis of daily precipitation as a function of station network density and found that the gauge analysis bias is negligible and the random error is only a fraction of that for the CMORPH satellite estimates over a 0.25° lat–lon grid box with one or more reporting gauges.

Figure 4 shows a comparison of long-term daily mean precipitation estimates derived from the raw CMORPH and the CPC gauge-based analysis for the entire data period from 1998 to 2015. The raw CMORPH (Fig. 4, middle left) presents mean precipitation of very similar spatial patterns to that of the CPC gauge analysis (Fig. 4, top right) over the global land. The centers of heavy rainfall over equatorial Africa, the Maritime Continent, and the Amazon associated with the intertropical convection zone (ITCZ) are well captured, together with the bands of precipitation over coastal regions attributable to the monsoon circulations, and over mid- and high-latitude regions of cyclone passage and frontal activities. The raw CMORPH, however, overestimates the precipitation over most of the tropical land areas, while underreporting the annual mean precipitation over mid- and high-latitude land areas, as shown in the difference map between the raw CMORPH and the CPC gauge (Fig. 4, bottom left).

A quantitative evaluation is carried out for the raw CMORPH over the contiguous United States (CONUS) through comparison against the high-quality CPC daily gauge analysis (Fig. 5). To ensure accurate evaluation, only daily precipitation analysis over a 0.25° lat–lon grid box with one or more reporting gauges is included in the bias examination. Averaged over the entire CONUS for the 18-yr period from 1998 to 2015, the raw CMORPH shows a distinct annual cycle of bias, over and underestimating precipitation over the warm and cold seasons, respectively (Fig. 5a). The biases in the raw CMORPH, and other integrated satellite precipitation (e.g., NASA TMPA) as well, are attributable to those in the input level 2 PMW retrievals (Xie and Joyce 2014). Previous studies indicate that the overestimation of warm season precipitation is mostly caused by overestimation for the precipitation intensity for precipitating cloud systems, while the underestimation for the cold seasons are combined effects of undetected precipitation events and undervalued intensity (Tian et al. 2009; Xie and Joyce 2014).

Raw CMORPH bias exhibits year-to-year variations, as shown in Fig. 5b, caused by interannual variability of the cloud and precipitation systems and by the changes in the PMW sensors aboard satellites indicated in Fig. 3.

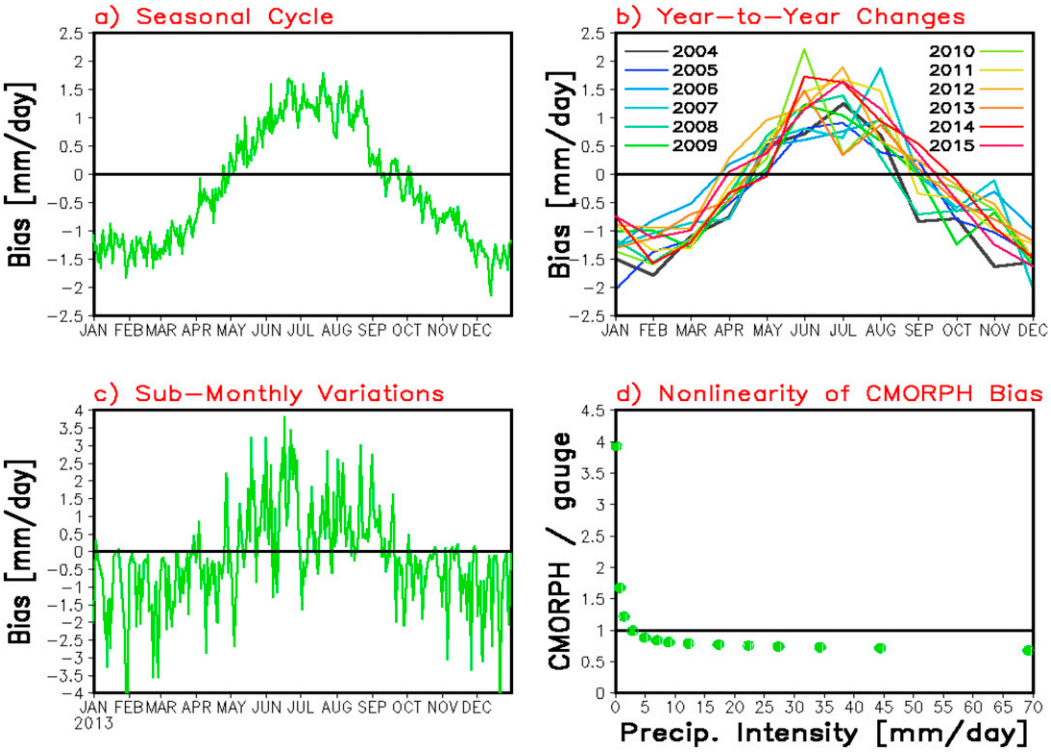


FIG. 5. Comparison of the raw CMORPH against the CPC Unified gauge analysis over CONUS. (a) Daily climatology of raw CMORPH bias averaged over the entire CONUS for the entire data period from 1998 to 2015. (b) Raw CMORPH monthly mean bias (mm day$^{-1}$) averaged over the entire CONUS for each year from 2004 to 2015. (c) Time series of raw CMORPH daily mean CMORPH averaged over the entire CONUS for 2013. (d) Raw CMORPH bias, expressed as the ratio between CMORPH and gauge analysis, as a function of precipitation intensity. Only the CMORPH–daily gauge data pairs over 0.25° lat–lon grid boxes where/when gauge reports are available from at least one station are included in the calculations.

Despite their sophisticated models reflecting the relationship between the surface precipitation and the radiance measurements from multiple PMW channels, modern-era PMW retrievals still suffer from different types of biases for different cloud/precipitation systems. Changes in the weather regimes therefore will yield biases in the retrieved precipitation. Different PMW sensors covering different parts of the data period may also cause differences in the precipitation retrievals due to the imperfect intercalibration.

The raw CMORPH also shows biases of submonthly time scales, even for precipitation averaged over the entire CONUS domain (Fig. 5c). The fluctuations of the biases are results of variable cloud–precipitation relationships for the individual weather systems. Overall, the raw CMORPH tends to overestimate weak precipitation while underreporting strong events, presenting nonlinearity in its bias structure as a function of the target precipitation intensity (Fig. 5d).

In summary, the raw CMORPH bias is regionally dependent, temporally changing, and is a nonlinear function of target precipitation intensity. While seasonal variations are quite significant in the raw CMORPH biases, with over and underestimation observed for warm and cold seasons, respectively, the bias also shows year-to-year variations as well as fluctuations of submonthly time scales.

### 2) ALGORITHM TO REMOVE CMORPH BIAS OVER LAND

Several of the published methods [e.g., Huffman et al. (2007) for TMPA and Ashouri et al. (2015) for PERSIANN CDR] apply spatially and temporally varying coefficients to adjust the raw satellite estimates, implicitly assuming linearity of the satellite estimation bias relative to the precipitation intensity. In addition, adjustment coefficients are computed against a reference field of monthly precipitation (e.g., GPCC monthly gauge or GPCP monthly merged analysis), assuming homogeneity of satellite estimation bias within a month. In our approach, both the nonlinearity and the submonthly variations of raw CMORPH bias are accounted for through matching the PDF of the daily raw CMORPH against that for the CPC daily gauge analysis.

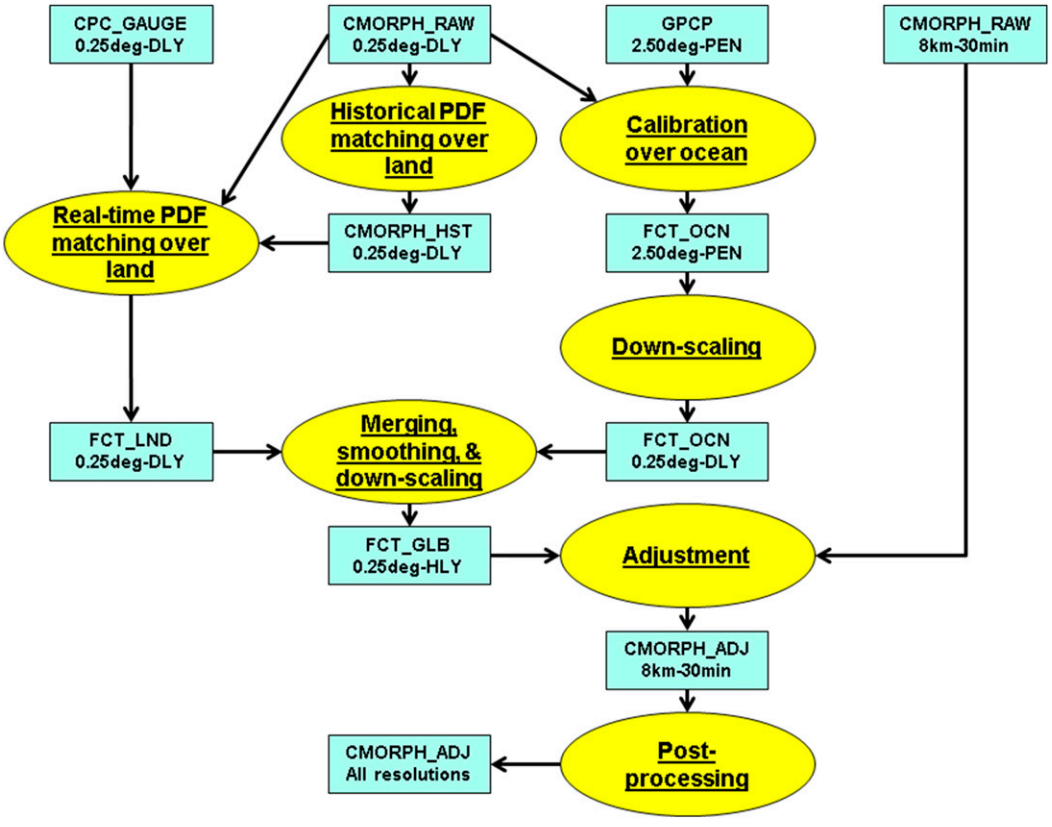


FIG. 6. Flowchart of the CMORPH bias correction procedures.

The PDF matching technique is capable of removing the bias in the mean value while ensuring the fidelity of the frequency distribution for events of various intensities (Haddad and Rosenfeld 1997; Turk et al. 2003; Wang and Xie 2007; Huffman et al. 2007; Xie et al. 2014). A conceptual model developed using the CMORPH and gauge data over China has demonstrated the feasibility of the PDF-matching-based bias-removal technique (Xie and Xiong 2011). The system described below is an operational realization of the technique to perform bias correction for the raw CMORPH over the global land areas.

Figure 6 illustrates the flowchart of the CMORPH bias correction system. The bias correction over land is implemented in two consecutive steps. First, bias correction is performed using PDF tables constructed with historical data (Fig. 6, top center-right). To account for the regional changes and seasonal evolution of the raw CMORPH bias structures, PDF tables are constructed for each grid box of 0.25° lat–lon and for each calendar day. Raw CMORPH and CPC daily gauge data are collected over a 31-day period, centering at the target date over the entire 15-yr period and over a circular spatial domain of two grid boxes (0.5° lat–lon) with the radius centered at the target grid box. The spatial domain is expanded to achieve at least 500 collocated data pairs with at least 300 cases of raw CMORPH reporting nonzero precipitation. The collected raw CMORPH and the CPC gauge data are then sorted separately in descending order and grouped into 100 equal numbered classes. The adjustment coefficient is calculated for each class as the ratio between the mean value of CPC gauge data and that of the raw CMORPH averaged over five consecutive classes centering at the target class. The two threshold numbers of cases (500/300) are determined empirically to ensure optimal balance between the stability and time–space representativeness for the resulting bias correction statistics. The bias correction is conducted through multiplying the raw CMORPH precipitation estimates with the adjustment coefficient. This first step of the bias correction is called climatological correction, intended to remove/reduce the mean bias reflected in the historical data.

The second step (Fig. 6, right), termed here as the real-time refinement, is designed to account for the year-to-year variations in the raw CMORPH bias not detected and removed by the climatological correction. The bias correction procedure is repeated but with the PDF tables established using collocated CMORPH and daily

gauge data for a 31-day period centered at the target date. PDF tables are constructed for each 0.25° lat–lon grid using data over a spatial domain expandable following the same criteria rules in the climatological correction. The result of this two-step bias correction approach is an array of correction coefficients on a 0.25° lat–lon grid over the global land computed for daily precipitation.

The PDF bias correction described above is unable to adjust a zero-value case to a positive precipitation without additional information. This will cause underestimation in the total precipitation amount in the PDF-corrected satellite precipitation. A ratio is calculated between the mean of the reference field and that of the PDF-corrected field and is applied back to the PDF-corrected fields, with a range limit of 0.95–1.05, to ensure the accuracy of the overall magnitude in the bias-corrected CMORPH.

The conceptual model for bias correction as described in Xie and Xiong (2011) contains only one step to perform PDF matching against concurrent gauge data (real-time correction). In applying the methodology to regions of very sparse gauge networks, such as equatorial Africa, collocated gauge–CMORPH data pairs need to be collected over a very large region of different weather regimes. The resulting PDF tables are therefore unable to accurately represent the CMORPH bias structure over the target grid box, causing large errors in the corrected CMORPH. The climatology correction is based on PDF tables constructed using data pairs collected over an extensive historical period and over a therefore much smaller spatial domain. Including the climatology correction as the first step of the bias correction procedure enables the quantification of CMORPH bias structure with PDF tables to be much more representative of the weather/climate conditions.

### b. CMORPH bias correction over ocean

No observations are available from gauges or other in situ platforms over the vast oceanic regions covering an extended period for use as a reference standard to remove the biases in the raw CMORPH. The purpose of this part of the work rather is to adjust the raw CMORPH against a homogeneous long-term record of oceanic precipitation so that the adjusted CMORPH is capable of providing climate information of fine structure precipitation over the global oceans.

In this study, the GPCP merged analysis of pentad precipitation (Xie et al. 2003) is used as the reference field to adjust the raw CMORPH over the ocean. The GPCP pentad analysis is defined on a 2.5° lat–lon grid over the globe through calibrating the pentad CPC Merged Analysis of Precipitation (CMAP; Xie and Arkin 1997) against the GPCP merged analysis of monthly precipitation, version 2 (Adler et al. 2003). The GPCP 1-degree daily (1DD) dataset (Huffman et al. 2001) provides a homogeneous long-term record of global precipitation at a fine space (time) scale [1° (daily)]. However it is not available on a real-time basis and therefore is not used in this work as the reference standard. The flowchart of the CMORPH oceanic bias correction procedures is illustrated in Fig. 6 (top center-left).

The raw CMORPH satellite estimates are first upscaled from their original resolution (8 km × 8 km and 30 min) to 2.5° lat–lon and pentad to match the GPCP merged analysis. Adjustment coefficient for the raw CMORPH is first calculated for each pentad time step and for each 2.5° lat–lon grid box as the ratio between the mean GPCP and mean raw CMORPH averaged over a circular region of three grid boxes of 2.5° lat–lon in radius and for a 19-pentad time period centering at the target grid box and target analysis time. The adjustment coefficient computed for each 2.5° lat–lon grid box and for each pentad period is then downscaled to daily and 0.25° lat–lon resolution, assuming no changes in the coefficient inside the 2.5° lat–lon grid box and within a pentad time period.

### c. Merging and downscaling the adjustment factors

The adjustment coefficients computed for land and ocean for daily precipitation are then merged into a combined global field with smooth transition over the land–sea boundaries. To this end, the adjustment factors over the coastal grid boxes are first smoothed to reduce discontinuities (Fig. 6, middle). The smoothing is performed over oceanic grid boxes within the distance of two 0.25° lat–lon grid boxes from any land points.

The global field of 0.25° lat–lon and daily resolution is then downscaled to create a global array of adjustment coefficients on an 8 km × 8 km and 30-min resolution. The raw CMORPH bias is nonlinear relative to the precipitation intensity, so the adjustment coefficient for each of the 48 half-hourly fields in a day is different from that for the daily mean precipitation, changing with the precipitation intensity (Xu et al. 2010). Ideally, this nonlinearity should be taken into account in downscaling the adjustment coefficients computed for daily precipitation over a 0.25° lat–lon grid box to a finer time–space resolution. A simplified approach is taken in this study to downscale the adjustment coefficients to 30-min and 8 km × 8 km resolution, assuming no changes in the adjustment coefficient inside a 0.25° lat–lon and daily box. Smoothing is then applied crossing the grid box and time step boundaries. The final bias-corrected CMORPH is defined by applying this downscaled adjustment coefficient to the raw CMORPH.

*d. Verifications of the bias-corrected CMORPH*

The bias-corrected CMORPH integrated satellite global precipitation estimates are generated for an 18-yr period from 1 January 1998 to 31 December 2015. An example of the bias-corrected CMORPH at 0000 UTC 1 August 2014 is illustrated in Fig. 2d. The spatial patterns of the bias-corrected CMORPH are almost exactly the same as those for the raw CMORPH (Fig. 2c), while differences of various magnitudes are observed, especially over mid- and high-latitude oceans. No discontinuities are visible across the land–sea boundaries. To demonstrate the effectiveness of the bias correction procedures described in the previous subsections, the raw and bias-corrected CMORPH satellite precipitation estimates are compared against ground observations and the GPCP merged analysis.

1) EFFECTIVENESS OF THE BIAS CORRECTION OVER LAND

The raw and bias-corrected CMORPH satellite precipitation estimates are compared against the CPC daily gauge analysis to quantify their performance over land. Although the CPC daily gauge analysis is used to calibrate the CMORPH and therefore is not fully independent of the bias-corrected CMORPH, the manner in which the PDF tables are constructed, however, greatly lowered the dependence of the bias-corrected CMORPH at a grid box on the gauge data over that same location. A simple examination with data over a limited area (China) showed little difference between performance statistics achieved through a direct comparison with this partially dependent gauge data and those computed through a complete cross validation with totally independent gauge data (not shown). Considering the magnitude of work involved in performing a full cross validation similar to the one described in Xie et al. (2007), here in this study, we examine the effectiveness of the bias correction through simple comparison against the CPC gauge data.

Figure 4 (right) presents a comparison of the 1998–2015 mean annual precipitation derived from the bias-corrected CMORPH against that for the CPC daily gauge analysis (Fig. 4, top right). Bias in the raw CMORPH over land, as shown in Fig. 4 (left), is greatly removed over most land areas with reasonable gauge coverage (Fig. 4, bottom right). Negative bias remains, with reduced magnitude, over middle and high latitudes over the Northern Hemisphere. This is caused by poor capacity of the input PMW retrievals in detecting snowfall and cold season rainfall, which will be discussed in more detail later in this subsection. The relatively large "bias" that appeared over equatorial Africa and along the western coast of South America is actually the result of the poor quality of gauge analysis. The distance between two nearby gauges may be 500 km or farther over equatorial Africa, while over South America, the sparse station networks often miss precipitation along the western slope of the Andes mountain range. The differences showing in those regions therefore are largely not the bias in the CMORPH. A simple comparison of the bias-corrected CMORPH with the gauge data over locations with reporting stations over the two regions, however, showed very close agreement (not shown).

To examine the effectiveness of the various algorithm components, two intermediate results of the bias correction procedures are used: CMORPH after adjustments with the climatology correction and CMORPH after the bias correction refinement with real-time data. Figures 7 (top and bottom) show the correlation and the bias between the CMORPH satellite estimates and the CPC daily gauge analysis as a function of season, respectively, while Fig. 8 presents time series of the two comparison statistics for the entire data period from 1998 to 2015. In both figures, comparisons are made for daily precipitation over the entire global land from 60°S to 60°N. Only data over a 0.25° lat–lon box with one or more reporting gauges are included in the calculations to ensure reliable examinations.

The PDF matching technique described in section 3a succeeded in removing the bias in the raw CMORPH over the land areas during the warm season (Fig. 7). While the climatological correction (red lines) substantially reduced the biases for all seasons, applying real-time refinement (green lines) further improved the performance of the bias-corrected CMORPH. Downscaling and smoothing the adjustment factor from daily and 0.25° lat–lon to 30 min and 8 km × 8 km enabled the bias correction at CMORPH's native resolution but resulted in a slight degradation in performance (blue lines). Overall, the bias is removed almost completely and the pattern correlation is increased by ~0.1 over warm seasons. Over cold seasons, bias remains, although its magnitude is reduced substantially. The imperfect performance of the bias correction procedure is caused by the limited detection capability of the input level 2 retrievals for cold season precipitation (Xie and Joyce 2014). The PDF technique is unable to raise a zero-value retrieval to a nonzero estimation. Key to the improvement of cold season precipitation estimates is the development and production of snowfall rate and cold season rainfall retrievals such

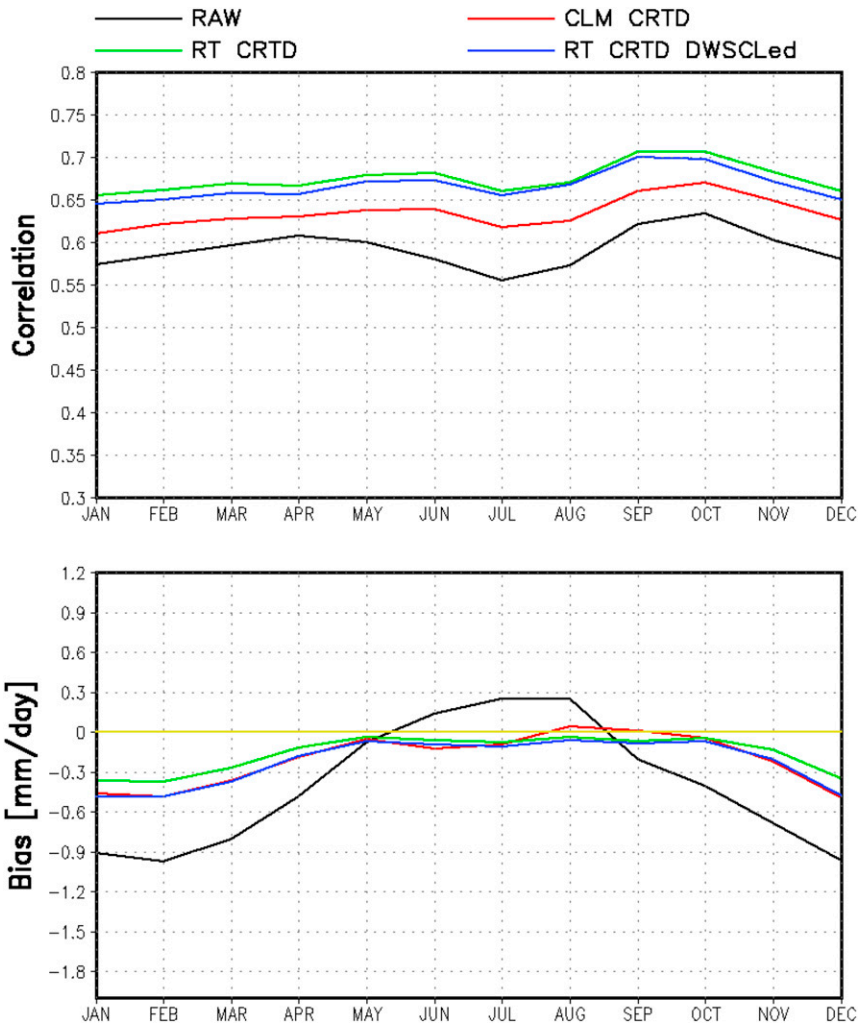


FIG. 7. (top) Correlation and (bottom) bias (mm day$^{-1}$) of the CMORPH precipitation estimates as a function of season. The two performance statistics are calculated through comparison against CPC Unified gauge analysis of daily precipitation on a 0.25° lat–lon grid over the global land for a 17-yr period from 1998 to 2015. Results for the raw, climatologically corrected, real-time enhanced, and bias-corrected–downscaled CMORPH are shown in black, red, green, and blue lines, respectively. Only gauge–CMORPH data pairs over 0.25° lat–lon grid boxes where/when reports are available from one or more stations are included in the calculations.

as those of Wang et al. (2009, 2011) and Meng et al. (2011).

Performance of the CMORPH satellite precipitation estimates improves with time as the number of the LEO platforms with PMW sensors increases, especially during the earlier half of the data period (Fig. 8). The correlation is ~0.50 and 0.55 for the raw and bias-corrected CMORPH during 1998–99, respectively, when PMW retrievals are available from only three LEO satellites. It reaches ~0.60 and 0.65 for period after 2006 when there are eight or more LEO platforms, as indicated in Fig. 3. As already clearly shown in Fig. 7, the bias in the raw CMORPH is removed almost completely over the warm seasons, while it is reduced substantially (Fig. 8, bottom) over cold seasons.

### 2) EFFECTIVENESS OF THE ADJUSTMENT OVER OCEAN

Over global oceans, the raw CMORPH is calibrated against the pentad GPCP analysis to ensure long-term homogeneity. To examine the performance of this adjustment, the calibrated CMORPH, created following the procedures described in section 3b, is upscaled from the CMORPH native resolution of 30 min and 8 km × 8 km

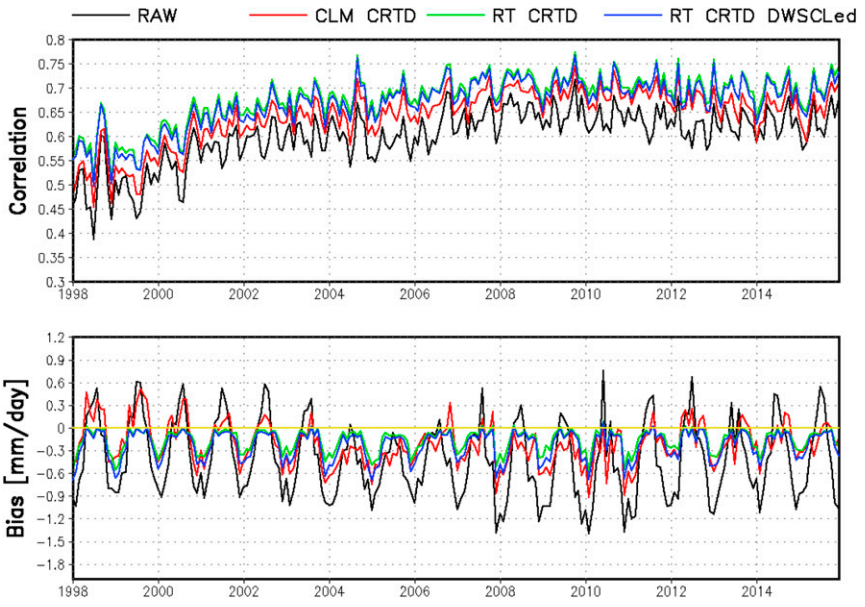


FIG. 8. As in Fig. 7, but for time series of the performance statistics. Correlation and bias are calculated for each month, from January 1998 to December 2015, using daily gauge and CMORPH data over 0.25° lat–lon grid boxes over the entire global land where/when reports are available from one or more stations are included in the calculations.

to a pentad and 2.5° lat–lon and compared against the pentad GPCP for the entire 18-yr period from 1998 to 2015. While the raw CMORPH (Fig. 9, middle left) exhibits very similar spatial patterns of long-term mean precipitation with the pentad GPCP analysis (Fig. 9, top right), it is wetter/drier than the GPCP merged analysis over tropical/high-latitude oceans (Fig. 9, bottom left). After the adjustment, CMORPH presents very close agreements with the pentad GPCP in both the distribution patterns and the precipitation magnitude (Figs. 9, middle right and bottom right). Underestimation of very small magnitude remains over high-latitude oceans close to the very northern and southern edges of the domain (Fig. 9, bottom right). This is due to the upper limit set for the adjustment factors (2.0) for pentad accumulation over a 2.5° lat–lon grid box to avoid unrealistic precipitation fields. Examinations of the CMORPH against independent in situ observations will be presented in the next section as part of the evaluation and intercomparison.

## 4. Evaluation and intercomparison

The reprocessed, bias-corrected CMORPH is evaluated against several high-quality ground truth datasets of surface precipitation and intercompared with a similar long-term time series of global high-resolution precipitation: TRMM 3B42 (TMPA), version 7. The primary objective of this part of the work is to quantify the performance of the bias-corrected CMORPH in depicting precipitation and its variations at various time–space scales.

### *a. Comparison with CPC daily gauge analysis over the global land*

First, the CMORPH and TMPA satellite precipitation estimates are compared against the CPC daily gauge analysis to examine the performance of the two satellite products in representing precipitation and its variations over the global land. The comparisons are conducted using data over 0.25° lat–lon grid boxes when/where both the CMORPH and TMPA are available and the CPC gauge analysis is created with reports from at least one station inside the target grid box. Figure 10 shows the time series of the pattern correlation (Fig. 10, top) and bias (mm day$^{-1}$; Fig. 10, bottom) for the two satellite products computed using data over the global land areas from 50°S to 50°N. The bias-corrected CMORPH exhibits consistently better pattern correlation throughout the data period from 1998 to 2015, indicating superior capability of CMORPH in depicting the spatial distribution patterns of daily precipitation. For both CMORPH and TMPA, correlation improves with time for the early part of the period when the number of LEO satellites carrying PMW sensors increases from three to seven. The correlation becomes stable from 2006 when there are more than seven satellites.

The bias-corrected CMORPH satellite precipitation estimates present an annual cycle in the bias against the

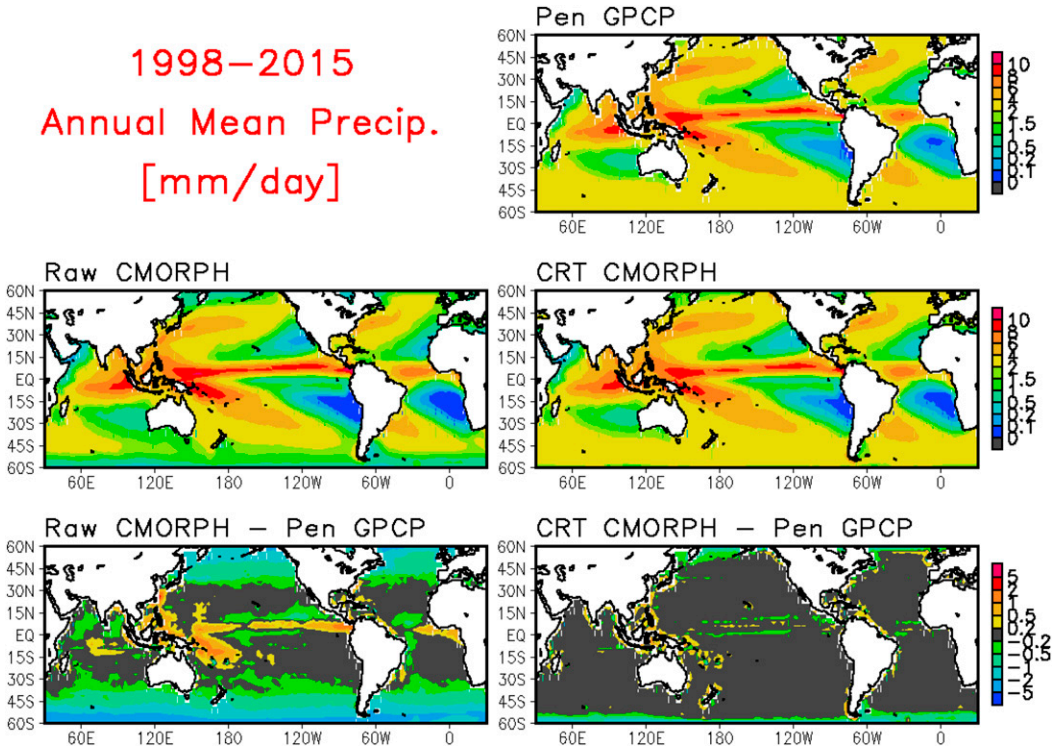


FIG. 9. The 1998–2015 annual mean precipitation (mm day$^{-1}$) for (top right) the GPCP pentad merged analysis, (middle left) the raw CMORPH, (middle right) the bias-corrected CMORPH, (bottom left) the differences between the raw CMORPH and the pentad GPCP, and (bottom right) the differences between the bias-corrected CMORPH and the pentad GPCP.

CPC gauge analysis, with minimum bias over the warm seasons and negative bias during cold seasons (black line in Fig. 11, bottom). As discussed in the previous section, this cold season underestimation in the CMORPH can be traced back to the detection deficiencies in the input level 2 PMW precipitation retrievals. The current generation PMW retrievals present poor skills in detecting and quantifying cold season precipitation, especially the snowfall. No annual cycle in the bias is observed for the TMPA, thanks to a procedure to force the monthly total precipitation to match the GPCC gauge analysis over land (Huffman and Bolvin 2014). The TMPA bias against the CPC daily gauge analysis, however, shows a slightly declining trend throughout the data period (red line in Fig. 10, bottom). A preliminary examination suggested that this negative trend in the TMPA bias against the CPC gauge analysis is caused by the differences in the GPCC monthly gauge and the CPC daily gauge analyses. More examinations are needed to explore the causes of this difference between the two gauge analyses.

No significant seasonal variations are observed in the pattern correlation between CMORPH/TMPA and gauge analysis when data over the entire global land are used in the calculation (Fig. 11, top). This is largely due to the inclusion of data from both the Southern and Northern Hemispheres. Overall, the correlation for CMORPH is ~0.05 higher than that for the TMPA. The TMPA shows a consistent slight overestimation (~0.2 mm day$^{-1}$) compared to the CPC daily gauge analysis throughout the annual cycle. CMORPH, however, tends to underestimate the precipitation during boreal winter, a reflection of less-than-desirable performance of CMORPH in picking up cold season precipitation over the Northern Hemisphere.

### b. *Comparison with NCEP stage IV radar precipitation estimates over CONUS*

The National Centers for Environmental Prediction (NCEP) stage IV radar precipitation estimates provide a high-quality reference standard for precipitation estimates over CONUS (Nelson et al. 2016). Regional analyses of hourly and 6-hourly precipitation are first constructed at the 12 National Weather Service (NWS) River Forecast Centers (RFC) over the CONUS through blending information from the radar estimates and gauge measurements with the Multisensor Precipitation Analysis (MPE) technique (Seo and Breidenbach 2002). These regional analyses are then

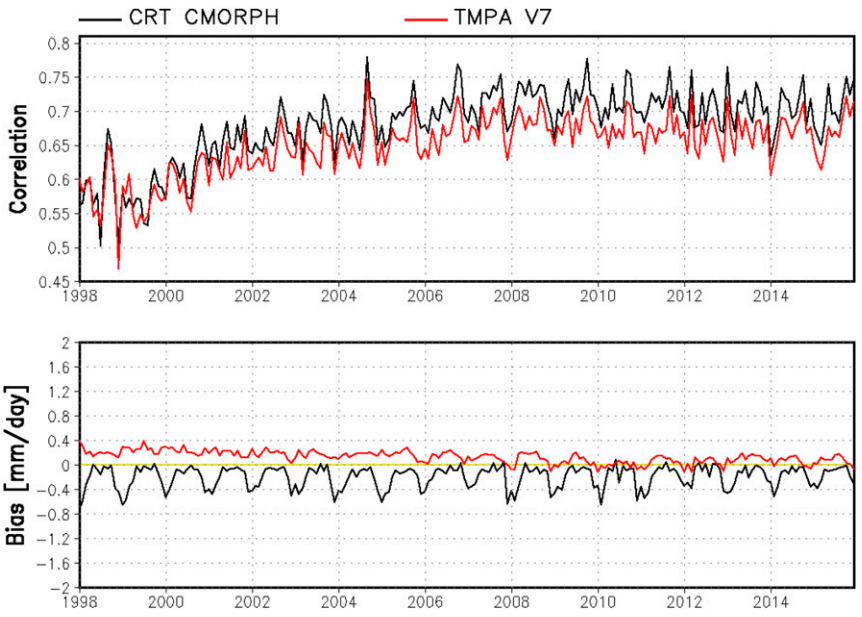


FIG. 10. Time series of the (top) correlation and (bottom) bias (mm day$^{-1}$) for the bias-corrected CMORPH (black) and TMPA, version 7 (red), over the entire data period from January 1998 to December 2015. The statistics are calculated for daily precipitation over a 0.25° lat–lon grid box through comparison against CPC Unified gauge analysis of daily precipitation over the global land (50°S–50°N). Only daily precipitation data over 0.25° lat–lon grid boxes where/when at least one reporting gauge is available are used to ensure reasonable quality of the gauge analysis.

mosaicked into a national product at the NCEP Environmental Modeling Center (EMC) on a quasi-real-time basis (Lin and Mitchell 2005; Nelson et al. 2016).

While CMORPH generates 30-min mean precipitation over an 8 km × 8 km grid box, time (space) resolution for TMPA is 3 hourly (0.25° lat–lon). In addition, the 3-hourly period for the TMPA precipitation estimates are centered at the eight synoptic hours so that the 3-hourly block stamped at 1200 UTC covers a 180-min period from 1030 to 1330 UTC. To ensure fair comparisons, 3-hourly CMORPH is assembled from the original 30-min CMORPH data following the TMPA definition of the time periods. Daily precipitation estimates are then computed from the 3-hourly data for CMORPH and TMPA, respectively.

The stage IV radar analysis of hourly precipitation, originally constructed on a 4 km × 4 km grid, is post-processed into an equal angle grid system of 0.25° lat–lon resolution to match the spatial resolution of TMPA. Since the stage IV hourly data are for a 60-min period ending at each hour, 3-hourly mean stage IV precipitation matching the TMPA definition is calculated as the weighted mean of four hourly values covering the target period, with the hourly data for the first and fourth hours receiving half of the weight as those for the two hours in the middle. For example, 3-hourly mean stage IV precipitation at 1200 UTC is the weighted mean of hourly values at 1000, 1100, 1200, and 1300 UTC, with weights of 0.5, 1.0, 1.0, and 0.5, respectively.

The CMORPH and TMPA satellite precipitation estimates are first validated against the stage IV radar data for all months throughout a 14-yr period from 2002 to 2015 (Fig. 12). As of July 2016, no stage IV data are available for periods before 2002. Correlation between the CMORPH/TMPA satellite estimates and stage IV radar data is quite low (<0.3) for both the daily and 3-hourly precipitation over the mountainous regions west of 110°W (Figs. 12, top and middle), while the magnitude of the radar precipitation is substantially lower than satellite data over the same region (Fig. 12, bottom). This poor agreement between the radar and satellite precipitation data is attributable mostly to the less-than-desirable quality of the stage IV radar data in detecting precipitation over the region caused by mountain blockage and radar beam overshooting.

East of 110°W, serial correlation between the CMORPH/TMPA and radar data is quite high for both the daily (Fig. 12, top) and the 3-hourly precipitation (Fig. 12, middle). Bias-corrected CMORPH exhibits consistently higher correlation with the radar observations over most of the central and eastern CONUS, indicating superior performance in capturing the temporal

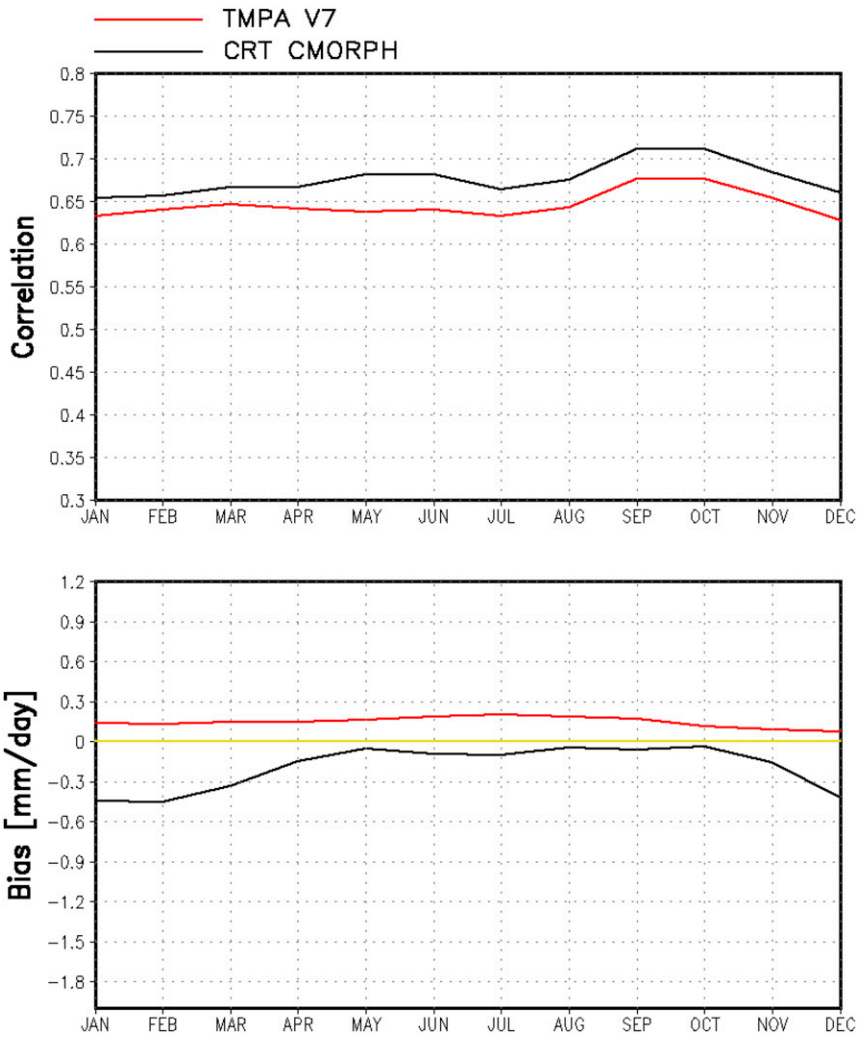


FIG. 11. Performance of the bias-corrected CMORPH (black) and TMPA, version 7 (red), in representing daily precipitation over a 0.25° lat–lon grid box over the global land as a function of season. (top) Correlation and (bottom) bias (mm day$^{-1}$) are calculated for each month through comparison against collocated CPC Unified gauge analysis of daily precipitation using data over the global land (50°S–50°N) for the entire data period from 1998 to 2015.

variations of precipitation at daily and subdaily time scales. Maximum correlation for CMORPH daily and 3-hourly precipitation estimates reaches >0.85 and >0.75 over central CONUS near the Gulf of Mexico coasts, respectively. The annual mean precipitation derived from TMPA shows a slight overestimation against the stage IV radar data over most of the central and eastern CONUS (Fig. 12, bottom right), a reflection that TMPA is adjusted by the GPCC monthly gauge analysis that is slightly different from the stage IV radar data. The 2002–15 annual mean precipitation from CMORPH, however, exhibits a spatially consistent underestimation over the northern portion of the domain (Fig. 12, bottom left). As discussed in the previous subsection, this is caused by the poor detection of the input level 2 PMW retrievals and thereby the CMORPH integrated estimates in capturing cold season precipitation, especially snowfall. As illustrated in Fig. 13, during the warm season [June–August (JJA)], both CMORPH and TMPA present improved performance with higher correlation and much smaller biases over most of the CONUS east of 110°W.

Performance of the bias-corrected CMORPH and TMPA over the CONUS east of 110°W is quite stable over the evaluation period from 2002 to 2015, although correlations for periods before 2007 are slightly lower than those for the period afterward, attributable to the difference in the number of PMW-equipped LEO satellites in operation (Fig. 14). Here again, the

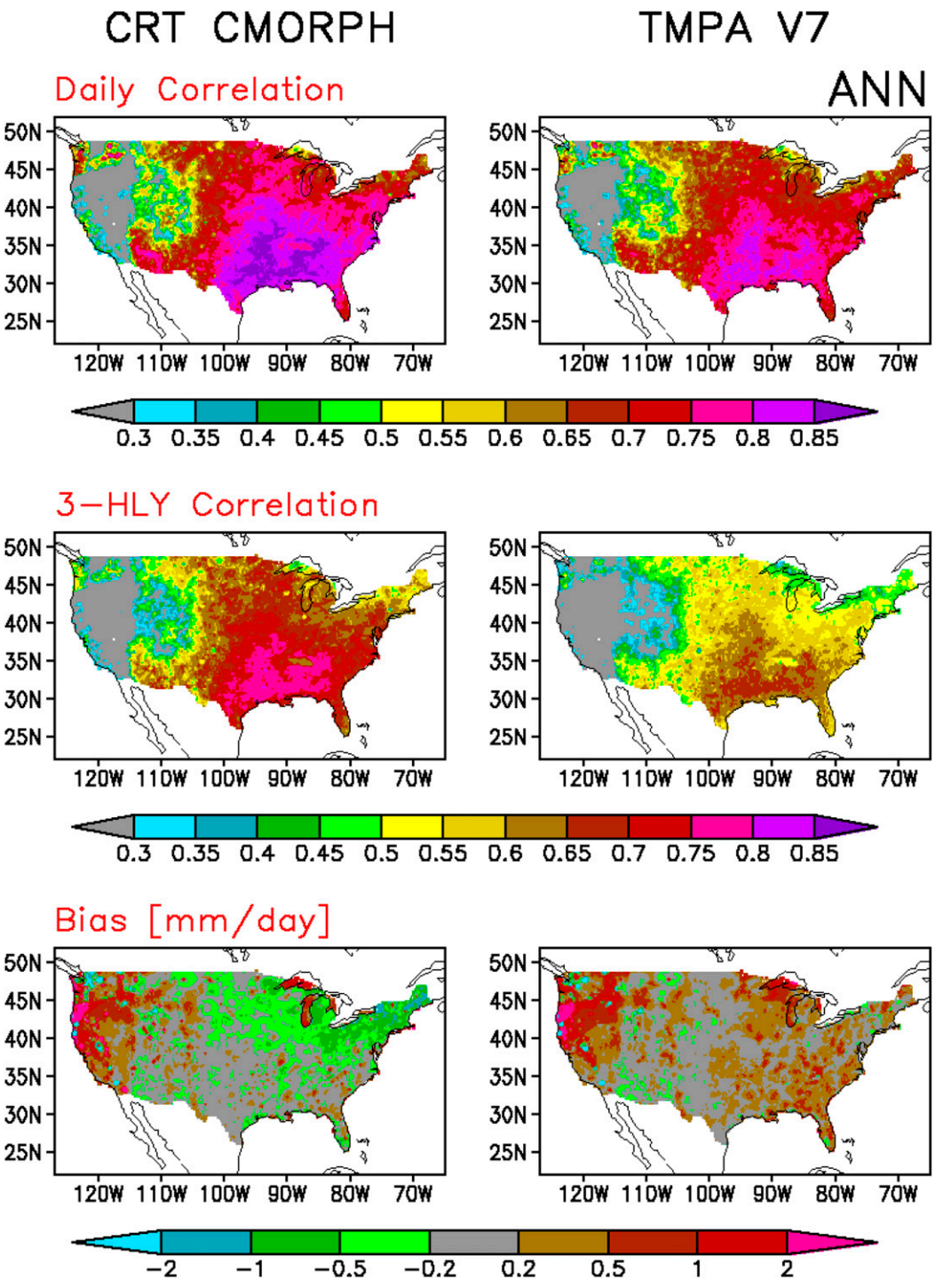


FIG. 12. Comparison statistics for the (left) CMORPH and (right) TMPA, version 7, precipitation estimates against the NCEP stage IV radar estimates. The statistics are computed for each grid box of 0.25° lat–lon grid over the CONUS using data for all 12 months over the entire data period from 1 Jan 2002 to 31 Dec 2015. Correlation for daily precipitation, 3-hourly precipitation, and bias (mm day$^{-1}$) are shown in the (top), (middle), and (bottom), respectively.

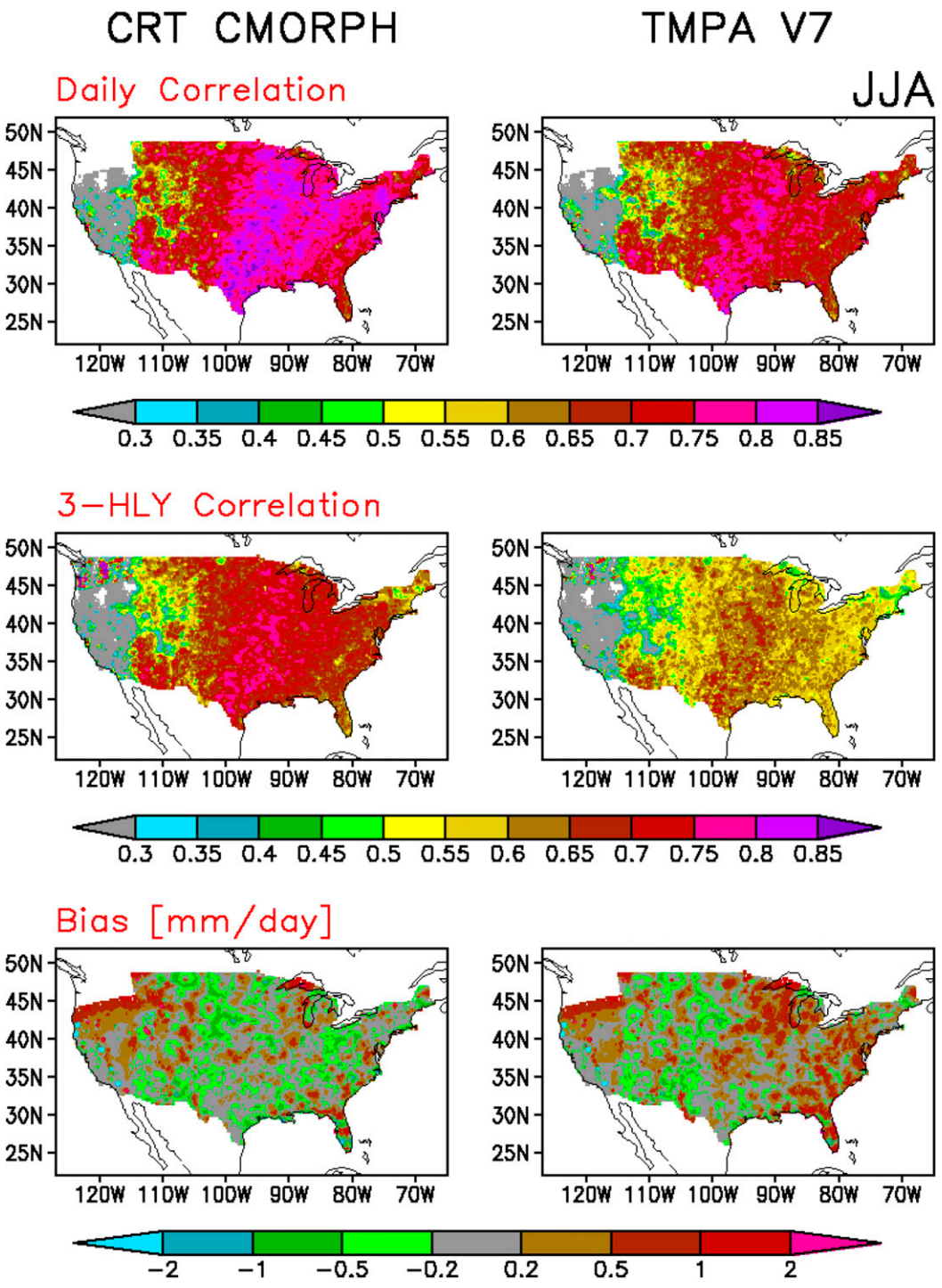


FIG. 13. As in Fig. 12, but for statistics computed using data for JJA from 2002 to 2015.

bias-corrected CMORPH exhibits a consistently higher pattern of correlation for both daily and 3-hourly precipitation, indicating a relatively superior capacity of the CMORPH in capturing the spatial patterns of precipitation over the region. A drop in correlation is observed around the end of 2002 and beginning of 2003 for both CMORPH and TMPA. Preliminary inspections showed that this is caused by suspicious radar precipitation around the western boundary (~110°W) over the evaluation domain.

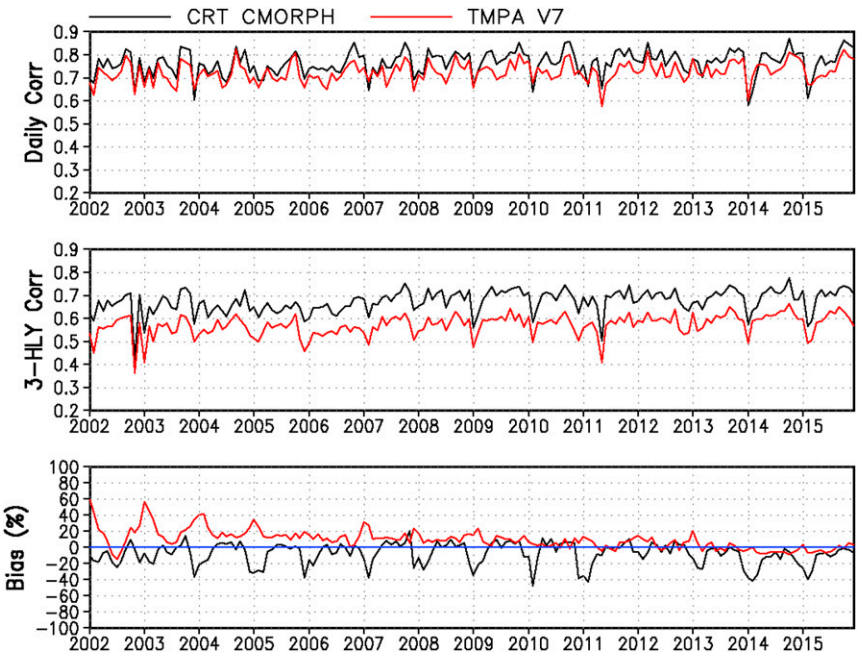


FIG. 14. Comparison statistics of the CMORPH (black) and TMPA, version 7 (red), precipitation estimates against the NCEP stage IV radar precipitation estimates. The statistics are computed as a function of time using data at 0.25° lat–lon grid boxes over the CONUS east of 110°W. Correlation for (top) daily precipitation, (middle) 3-hourly precipitation, and (bottom) bias (%; relative to the radar precipitation) are shown.

CMORPH presents an annual cycle of bias for precipitation estimates averaged over the entire evaluation domain, with an underestimation observed over winters as discussed before (Fig. 14, bottom). No significant bias is observed for TMPA over the CONUS for years after 2006. Overestimates, however, are visible for TMPA during cold seasons before 2005. In addition, the TMPA shows a negative trend in its bias against the stage IV radar data over the examination period from 2002 to 2015. Since the stage IV radar precipitation data are calibrated against the SYNOP gauge measurements used as part of the inputs to construct the CPC daily gauge analysis, this declining trend should be also caused by the systematic differences between the GPCC monthly gauge and the daily gauge data as discussed in section 4a.

Table 3 lists comparison statistics computed for the bias-corrected CMORPH and TMPA precipitation estimates at 0.25° lat–lon grid resolution over the CONUS east of 110°W and for the entire evaluation period from 2002 to 2015. CMORPH presents higher correlation than the TMPA for both daily and 3-hourly precipitation. Correlation coefficients for CMORPH are 0.761 and 0.671 for daily and 3-hourly precipitation, respectively, while they are 0.715 and 0.566 for TMPA. Since CMORPH is constructed on a 30-min temporal resolution, hourly CMORPH is created and compared against the stage IV radar data. A quite high correlation of 0.580 is achieved for the CMORPH hourly precipitation estimates, demonstrating good skill of the CMORPH data in resolving variations of subdaily time scales such as the evolution of mesoscale systems and the diurnal cycle. Both the CMORPH and the TMPA possess relatively small biases of less than 10% against the stage IV radar data.

### c. *Comparison with in situ measurements from moored buoys over tropical oceans*

Evaluation of high-resolution satellite precipitation products over ocean has been a challenging task because of the lack of appropriate surface observations used as the ground truth. While rainfall observations made by gauges at atolls and small islands (Morrissey et al. 1995) have been widely used to quantify the performance of satellite precipitation products of climate scale (e.g., Xie and Arkin 1995), their representativeness for precipitation of higher temporal–spatial scales over nearby open-ocean grid boxes is greatly compromised. Radar-based observations, like those produced by the ground validation components of the TRMM and GPM missions (Wolff et al. 2005), provide reliable precipitation estimation over a relatively broad spatial domain

TABLE 3. Comparison statistics of the CMORPH/TMPA satellite precipitation estimates against the NOAA/NCEP stage IV radar precipitation over the CONUS east of 115°W.

| Technique | Statistics | Daily 0.25° lat–lon | 3-hourly 0.25° lat–lon | Hourly 0.25° lat–lon |
|---|---|---|---|---|
| CMORPH | Correlation | 0.761 | 0.671 | 0.580 |
| | Bias (%) | −6.0 | −5.2 | −3.8 |
| TMPA | Correlation | 0.715 | 0.566 | — |
| | Bias (%) | 8.1 | 6.5 | — |

(~150 km in diameter) over ocean, but they are available only for short periods.

In this study, we take advantage of the rainfall measurements made from moored ocean buoys to examine the performance of the CMORPH and TMPA satellite precipitation products over tropical oceans. The buoy-measured precipitation data used here include those from the Tropical Atmosphere Ocean (TAO)/Triangle Trans-Ocean Buoy Network (TRITON) over the Pacific (McPhaden et al. 1998), the Prediction and Research Moored Array in the Tropical Atlantic (PIRATA) over the Atlantic (Bourles et al. 2008), and the Research Moored Array for African–Asian–Australian Monsoon Analysis and Prediction (RAMA) over the Indian Ocean (McPhaden et al. 2009). Reports of buoy measurements are collected and processed at the TAO Project Office at NOAA Pacific Marine Environmental Laboratory (PMEL) and released to general public.

Although buoy measurements of tropical oceanic rainfall are also available at finer temporal resolutions, only daily total precipitation data are used to ensure the best possible quality. Completed in 1994, TAO/TRITON provides precipitation reports from ~40 buoys, covering the equatorial Pacific across the entire basin. The number of PIRATA buoys with rainfall measurements, meanwhile, increased from ~8 for the earlier period before 2005 to ~14 for later years, reflecting an enhancement to the network in 2005. Newest in the global moored buoy network family, RAMA started operations in late 2004, achieving rainfall measurements from 12 to 18 sites for late years.

Since all of these buoys are moored at locations on the edges of the 0.25° lat–lon grid boxes of the CMORPH and TMPA satellite estimates, daily mean satellite precipitation over a 0.5° lat–lon grid box centering at the buoy locations is calculated and compared against the corresponding buoy measurements. A summary of the comparison statistics is given in Table 4. Both CMORPH and TMPA present very good skills in estimating daily precipitation and its variations over the tropical oceans, with CMORPH presenting slightly better performance statistics than TMPA. The overall bias is 4.4% for CMORPH and 16.7% for TMPA, while the correlation ranges from 0.583 to 0.684 for the CMORPH and from 0.564 to 0.669 for the TMPA. Here again, the bias-corrected CMORPH outperforms TMPA in representing the temporal–spatial variations of precipitation over the tropical oceans.

Relatively sparsely distributed buoy networks make it difficult to examine the regional dependence of the satellite precipitation performance. Instead, we calculated the serial correlation between CMORPH/TMPA and the buoy rainfall for each buoy location and examined the correlation variations as a function of the mean rainfall intensity measured by buoys (Fig. 15). Only results for buoy locations with 1000 or more days of collocated satellite–buoy data pairs are displayed to avoid fluctuations in the statistics caused by insufficient data. Correlation between satellite estimates and buoy measurements is quite stable, around 0.6–0.7, for locations with heavy rainfall, suggesting stable performance of CMORPH and TMPA in their capability to capture and quantify strong convective precipitation over tropical oceans. The spread in correlation, however, is quite large, ranging from 0.3 to higher than 0.8, for locations of light rainfall. Locations of light rainfall are associated with cloud systems of smaller spatial extension and shorter life span. The wide spread in the correlation is likely attributable to the combined effects of 1) less-than-excellent performance for the satellite retrieval algorithms to estimate instantaneous rain rates of weak intensity (Xu et al. 2015) and for the integration techniques to capture the evolution of a cloud system of shorter life span and 2) large error of the point measurements at buoy locations to represent mean precipitation over a 0.5° lat–lon grid box.

TABLE 4. Comparison statistics of the CMORPH/TMPA daily precipitation against buoy measurements from the TAO/TRITON, RAMA, and PIRATA networks.

| Technique | Statistics | TAO/TRITON (Pacific) | RAMA (Indian) | PIRATA (Atlantic) | All |
|---|---|---|---|---|---|
| CMORPH | Correlation | 0.684 | 0.583 | 0.642 | 0.653 |
| | Bias (%) | 5.1 | 12.7 | −6.6 | 4.4 |
| TMPA | Correlation | 0.669 | 0.564 | 0.637 | 0.640 |
| | Bias (%) | 16.6 | 26.0 | 7.4 | 16.7 |

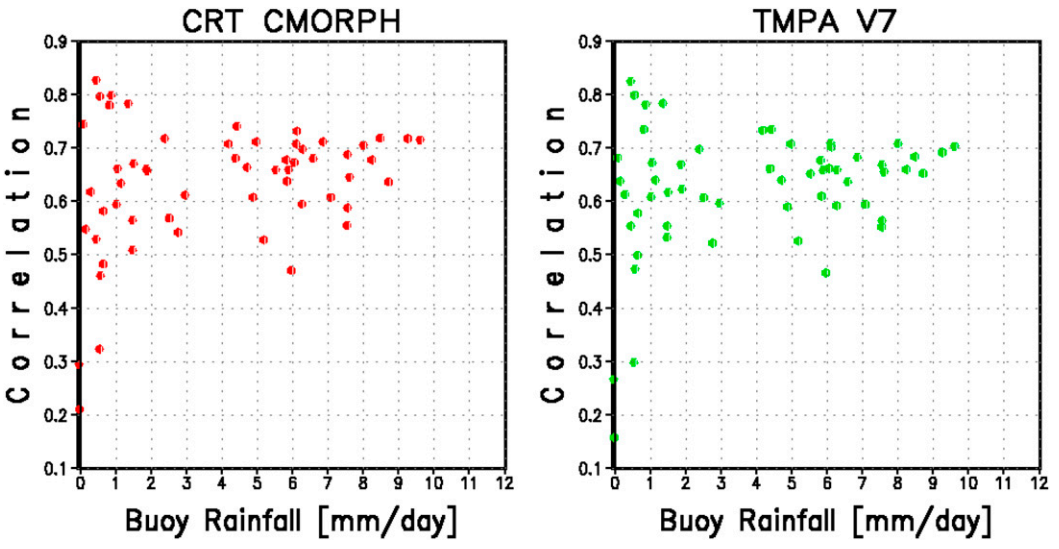


FIG. 15. Correlation between the CMORPH/TMPA satellite estimates of daily precipitation and buoy measurements from the TAO/TRITON, RAMA, and PIRATA networks, plotted as a function of mean buoy rainfall intensity. (left) CMORPH and (right) TMPA satellite precipitation rates are averaged over a 0.5° lat–lon grid box centering at buoy locations before they are compared with the buoy rainfall.

## 5. Summary and conclusions

The CMORPH global high-resolution satellite precipitation estimates have been reprocessed and bias-corrected on an 8 km × 8 km grid over the globe (60°S–60°N) for an 18-yr period from January 1998 to the present. First, the purely satellite-based CMORPH precipitation estimates have been reprocessed using a fixed version of the integration algorithm and with input from level 2 PMW retrievals of identical versions throughout the entire data period. The CMORPH integration technique used here is the version 1 algorithm described in Joyce et al. (2004), implementation as of 2009. The level 2 PMW retrievals are produced with GPROF, version 2004.

Bias correction is performed for the raw CMORPH through calibration against the CPC daily gauge analysis over land and against the GPCP pentad merged analysis of precipitation over ocean. The calibration over land is conducted by matching the PDF of the raw CMORPH satellite estimates against that of the temporally/spatially collocated CPC gauge analysis. The adjustment to the pentad GPCP analysis over ocean is carried out by applying correction coefficients defined as the ratio between the mean GPCP and mean raw CMORPH calculated locally and updated for each pentad.

The reprocessed, bias-corrected CMORPH exhibits improved performance in representing the magnitude, spatial distribution patterns, and temporal variations of precipitation over the global domain from 60°S to 60°N. Bias in the CMORPH satellite precipitation estimates is almost removed over land during the warm season, while during cold seasons CMORPH tends to underestimate the precipitation because of the less-than-desirable performance of the current-generation PMW retrievals in detecting and quantifying frozen precipitation and cold season rainfall.

An intercomparison study showed that the reprocessed, bias-corrected CMORPH exhibits consistently superior performance over the widely used TRMM 3B42 (TMPA) in representing the spatial–temporal variations for both the daily and 3-hourly precipitation over CONUS and other global regions. In particular, CMORPH is capable of capturing and quantifying subdaily variations of warm season precipitation, allowing potential applications of the satellite-based dataset in examining diurnal cycles and their representations in numerical models.

A major shortcoming of the current version of CMORPH is its less-than-desirable performance in detecting snowfall and cold season rainfall, causing a negative bias in the CMORPH over mid- and high-latitude land regions over cold seasons. Future improvements are expected, with the next version of CMORPH (Xie and Joyce 2014) to take in retrievals of snowfall rate such as those of Meng et al. (2011).

The bias-corrected CMORPH (called CMORPH, version 1.0, CRT) is updated on a quasi-real-time basis at NOAA/CPC. The data files are available through FTP (ftp.cpc.ncep.noaa.gov/precip/CMORPH_V1.0/CRT). Work

is underway to convert the bias-corrected CMORPH described in this paper into a CDR following required technical standards.

A global precipitation dataset created using a fixed version of integration algorithm and identical versions of inputs provides a homogeneous long-term record for climate applications. In the meantime, it is equally important that products of refined quality are developed by taking advantage of advanced technology and newly available satellite measurements. In particular, efforts are being made to improve the precipitation estimates using measurements from GPM (Huffman et al. 2011) and to expand the spatial coverage to polar regions (Xie and Joyce 2014).

Work is also underway to further combine the bias-corrected CMORPH with the CPC daily gauge analysis with a blending algorithm proposed by Xie and Xiong (2011). The gauge–CMORPH blended analysis will provide an analyzed field of daily precipitation over a 0.25° lat–lon grid resolution over the entire global land, with refined quantitative accuracy taking advantage of the strength of both the gauge measurements and satellite observations.

*Acknowledgments.* The work reported in this paper is carried out at the NOAA Climate Prediction Center (CPC) under joint support from NOAA/Climate Program Office (CPO) Climate Monitoring and Observations Program (Grant N8R1JRSP00); Ocean Climate Observation (OCO) Program; NOAA United States Weather Research Program (USWRP) Hydrometeorology Testbed (HMT, Grant K8R1RP5P01); and the NOAA National Environmental Satellite, Data, and Information Service (NESDIS) National Centers for Environmental Information (NCEI) Climate Data Record (CDR) Program. Comments and suggestions by Dr. K. Trenberth of National Center for Atmospheric Research (NCAR), Drs. Shi-Ken Yang and Wei Shi of NOAA/CPC, and three anonymous reviewers helped improve the quality of our work and the manuscript.

## REFERENCES

Adler, R. F., and Coauthors, 2003: The version-2 Global Precipitation Climatology Project (GPCP) monthly precipitation analysis (1979–present). *J. Hydrometeor.*, **4**, 1147–1167, doi:10.1175/1525-7541(2003)004<1147:TVGPCP>2.0.CO;2.

Armstrong, R. L., and M. J. Brodzik, 2002: Northern Hemisphere EASE-Grid weekly snow cover and sea ice extent version 2. National Snow and Ice Data Center, CD-ROM.

Ashouri, H., K.-L. Hsu, S. Sorooshian, D. K. Braithwaite, K. R. Knapp, L. D. Cecil, B. R. Nelson, and O. P. Prat, 2015: PERSIANN-CDR: Daily precipitation climate data record from multisatellite observations for hydrological and climate studies. *Bull. Amer. Meteor. Soc.*, **96**, 69–83, doi:10.1175/BAMS-D-13-00068.1.

Bates, J. J., and B. R. Barkstrom, 2006: A maturity model for satellite-derived climate data records. *14th Conf. on Satellite Meteorology and Oceanography*, Atlanta, GA, Amer. Meteor. Soc., P2.11. [Available online at https://ams.confex.com/ams/Annual2006/techprogram/paper_100658.htm.]

Becker, A., P. Finger, A. Meyer-Christoffer, B. Rudolf, K. Schamm, U. Schneider, and M. Ziese, 2013: A description of the global land-surface precipitation data products of the Global Precipitation Climatology Centre with sample applications including centennial (trend) analysis from 1901–present. *Earth Syst. Sci. Data*, **5**, 71–99, doi:10.5194/essd-5-71-2013.

Bourles, B., and Coauthors, 2008: The PIRATA program: History, accomplishments, and future directions. *Bull. Amer. Meteor. Soc.*, **89**, 1111–1125, doi:10.1175/2008BAMS2462.1.

Cosgrove, B. A., and Coauthors, 2003: Real-time and retrospective forcing in the North American Land Data Assimilation System (NLDAS) project. *J. Geophys. Res.*, **108**, 8842, doi:10.1029/2002JD003118.

Ebert, E. E., J. E. Janowiak, and C. Kidd, 2007: Comparison of near-real-time precipitation estimates from satellite observations and numerical models. *Bull. Amer. Meteor. Soc.*, **88**, 47–64, doi:10.1175/BAMS-88-1-47.

Ferraro, R., and Coauthors, 2005: NOAA operational hydrological products derived from the Advanced Microwave Sounding Unit (AMSU). *IEEE Trans. Geosci. Remote Sens.*, **43**, 1036–1049, doi:10.1109/TGRS.2004.843249.

Habib, E., A. T. Haile, Y. Tian, and R. J. Joyce, 2012: Evaluation of the high-resolution CMORPH satellite rainfall product using dense rain gauge observations and radar-based estimates. *J. Hydrometeor.*, **13**, 1784–1798, doi:10.1175/JHM-D-12-017.1.

Haddad, Z. S., and D. Rosenfeld, 1997: Optimality of empirical *Z–R* relations. *Quart. J. Roy. Meteor. Soc.*, **123**, 1283–1293, doi:10.1002/qj.49712354107.

——, E. A. Smith, C. D. Kummerow, T. Iguchi, M. R. Farrar, S. L. Durden, M. Alves, and W. S. Olson, 1997: The TRMM "Day-1" radar/radiometer combined rain-profiling algorithm. *J. Meteor. Soc. Japan*, **75**, 799–809.

Helfrich, S. R., D. McNamara, B. H. Ramsay, T. Baldwin, and T. Kasheta, 2007: Enhancements to, and forthcoming developments to the Interactive Multisensor Snow and Ice Mapping System (IMS). *Hydrol. Processes*, **21**, 1576–1586, doi:10.1002/hyp.6720.

Hong, Y., R. F. Adler, A. J. Negri, and G. J. Huffman, 2007: Flood and landslide applications of high-resolution satellite rainfall products. *J. Nat. Hazards*, **43**, 285–294, doi:10.1007/s11069-006-9106-x.

Hou, A. Y., and Coauthors, 2010: The Global Precipitation Measurement Mission. *Bull. Amer. Meteor. Soc.*, **95**, 701–722, doi:10.1175/BAMS-D-13-00164.1.

Hsu, K.-L., X. Gao, S. Sorooshian, and V. Gupta, 1997: Precipitation Estimation from Remotely Sensed Information Using Artificial Neural Networks. *J. Appl. Meteor.*, **36**, 1176–1190, doi:10.1175/1520-0450(1997)036<1176:PEFRSI>2.0.CO;2.

Huffman, G. J., and D. T. Bolvin, 2014: TRMM and other data precipitation data set documentation. NASA TRMM Doc., 42 pp. [Available online at ftp://precip.gsfc.nasa.gov/pub/trmmdocs/3B42_3B43_doc.pdf.]

——, R. F. Adler, M. Morrissey, D. T. Bolvin, S. Curtis, R. Joyce, B. McGavock, and J. Susskind, 2001: Global precipitation at

one-degree daily resolution from multi-satellite observations. *J. Hydrometeor.*, **2**, 36–50, doi:10.1175/1525-7541(2001)002<0036:GPAODD>2.0.CO;2.

——, ——, D. T. Bolvin, G. Gu, E. J. Nelkin, K. P. Bowman, E. F. Stocker, and D. B. Wolff, 2007: The TRMM Multisatellite Precipitation Analysis (TMPA): Quasi-global, multiyear, combined-sensor precipitation estimates at fine scales. *J. Hydrometeor.*, **8**, 38–55, doi:10.1175/JHM560.1.

——, and Coauthors, 2011: GPM Day-1 Multi-satellite algorithms (iMERG). *2011 PMM Science Team Meeting*, Denver, CO, NASA. [Available online at https://pmm.nasa.gov/meetings/all/2011-pmm-science-team-meeting.]

Jaeger, L., 1976: Monatskarten des Niederschiags fur die ganze Erde. Berichte des Deutscher Wetterdienstes, 33 pp.

Janowiak, J. E., R. J. Joyce, and Y. Yarosh, 2001: A real-time global half-hourly pixel-resolution IR dataset and its applications. *Bull. Amer. Meteor. Soc.*, **82**, 205–217, doi:10.1175/1520-0477(2001)082<0205:ARTGHH>2.3.CO;2.

Joyce, R. J., and P. Xie, 2011: Kalman filter–based CMORPH. *J. Hydrometeor.*, **12**, 1547–1563, doi:10.1175/JHM-D-11-022.1.

——, J. E. Janowiak, P. A. Arkin, and P. Xie, 2004: CMORPH: A method that produces global precipitation estimates from passive microwave and infrared data at high spatial and temporal resolution. *J. Hydrometeor.*, **5**, 487–503, doi:10.1175/1525-7541(2004)005<0487:CAMTPG>2.0.CO;2.

Kummerow, C., and Coauthors, 2001: The evolution of the Goddard profiling algorithm (GPROF) for rainfall estimation from passive microwave sensors. *J. Appl. Meteor.*, **40**, 1801–1820, doi:10.1175/1520-0450(2001)040<1801:TEOTGP>2.0.CO;2.

Leese, J. A., C. S. Novak, and B. B. Clark, 1971: An automated technique for obtaining cloud motion from geosynchronous satellite data using cross correlation. *J. Appl. Meteor.*, **10**, 118–132, doi:10.1175/1520-0450(1971)010<0118:AATFOC>2.0.CO;2.

Legates, D. R., and C. J. Willmott, 1990: Mean seasonal and spatial variability in gauge corrected global precipitation. *Int. J. Climatol.*, **10**, 111–127, doi:10.1002/joc.3370100202.

Lin, Y., and K. E. Mitchell, 2005: The NCEP stage II/IV hourly precipitation analyses: Development and applications. *19th Conf. on Hydrology*, San Diego, CA, Amer. Meteor. Soc., 1.2. [Available online at http://ams.confex.com/ams/Annual2005/techprogram/paper_83847.htm.]

McPhaden, M. J., and Coauthors, 1998: The Tropical Ocean–Global Atmosphere (TOGA) observing system: A decade of progress. *J. Geophys. Res.*, **103**, 14 169–14 240, doi:10.1029/97JC02906.

——, and Coauthors, 2009: RAMA: The Research Moored Array for African–Asian–Australian Monsoon Analysis and Prediction. *Bull. Amer. Meteor. Soc.*, **90**, 459–480, doi:10.1175/2008BAMS2608.1.

Mega, T., T. Ushio, T. Kubota, M. Kachi, K. Aonashi, and S. Shige, 2014: Gauge adjusted global satellite mapping of precipitation (GSMaP_Gauge). *XXXIth URSI General Assembly and Scientific Symp.*, Beijing, China, IEEE, 1–4, doi:10.1109/URSIGASS.2014.6929683.

Meng, H., R. F. Ferraro, and B. Yan, 2011: Satellite remote sensing of snowfall rate. *2011 PMM Science Team Meeting*, Denver, CO, NASA. [Available online at https://pmm.nasa.gov/meetings/all/2011-pmm-science-team-meeting.]

Meng, J., R. Yang, H. Wei, M. Ek, G. Gayno, P. Xie, and K. Mitchell, 2012: The land surface analysis in the NCEP Climate Forecast System Reanalysis. *J. Hydrometeor.*, **13**, 1621–1630, doi:10.1175/JHM-D-11-090.1.

Morrissey, M. L., M. A. Shafer, S. E. Postawko, and B. Gibson, 1995: The Pacific rain gauge rainfall database. *Water Resour. Res.*, **31**, 2111–2113, doi:10.1029/95WR01233.

Nelson, B. R., O. P. Prat, D.-J. Seo, and E. Harib, 2016: Assessment and implications of NCEP stage IV quantitative precipitation estimates for product intercomparisons. *Wea. Forecasting*, **31**, 371–394, doi:10.1175/WAF-D-14-00112.1.

Sapiano, M. R. P., and P. A. Arkin, 2009: An intercomparison and validation of high-resolution satellite precipitation estimates with 3-hourly gauge data. *J. Hydrometeor.*, **10**, 149–166, doi:10.1175/2008JHM1052.1.

Schneider, U., A. Becker, P. Finger, A. Meyer-Christoffer, M. Ziese, and B. Rudolf, 2014: GPCC's new land surface precipitation climatology based on quality-controlled in situ data and its role in quantifying the global water cycle. *Theor. Appl. Climatol.*, **115**, 15–40, doi:10.1007/s00704-013-0860-x.

Seo, D.-J., and J. P. Breidenbach, 2002: Real-time correction of spatially nonuniform bias in radar rainfall data using rain-gauge measurements. *J. Hydrometeor.*, **3**, 93–111, doi:10.1175/1525-7541(2002)003<0093:RTCOSN>2.0.CO;2.

Sevruk, B., 1982: Methods of correction for systematic error in point precipitation measurement for operational use. Operational Hydrology Rep. 589, WMO, 91 pp.

Simpson, J., R. F. Adler, and G. R. North, 1988: A proposed Tropical Rainfall Measuring Mission (TRMM) satellite. *Bull. Amer. Meteor. Soc.*, **69**, 278–295, doi:10.1175/1520-0477(1988)069<0278:APTRMM>2.0.CO;2.

Tang, L., Y. Tian, and X. Lin, 2014: Validation of precipitation retrievals over land from satellite-based passive microwave sensors. *J. Geophys. Res. Atmos.*, **119**, 4546–4567, doi:10.1002/2013JD020933.

Tian, Y., and Coauthors, 2009: Component analysis of errors in satellite-based precipitation estimates. *J. Geophys. Res.*, **114**, D24101, doi:10.1029/2009JD011949.

Turk, F. J., E. E. Ebert, B.-J. Sohn, H.-J. Oh, V. Levizzani, E. A. Smith, and R. Ferraro, 2003: Validation of an operational global precipitation analysis at short time scales. *12th Conf. on Satellite Meteorology and Oceanography*, Long Beach, CA, Amer. Meteor. Soc., JP1.2. [Available online at https://ams.confex.com/ams/annual2003/techprogram/paper_56865.htm.]

——, S. Miller, and C. Castello, 2010: A dynamic global cloud layer for virtual globes. *Int. J. Remote Sens.*, **31**, 1897–1914, doi:10.1080/01431160902926657.

Ushio, T., and Coauthors, 2009: A Kalman filter approach to the Global Satellite Mapping of Precipitation (GSMaP) from combined passive microwave and infrared radiometric data. *J. Meteor. Soc. Japan*, **87A**, 137–151, doi:10.2151/jmsj.87A.137.

——, and Coauthors, 2013: Global Satellite Mapping of Precipitation (GSMaP) project. *Int. Water Technol. J.*, **3**, 192–196.

Wang, N.-Y., C. Liu, R. Ferraro, D. Wolff, E. Zipser, and C. Kummerow, 2009: TRMM 2A12 land precipitation product—Status and future plans. *J. Meteor. Soc. Japan*, **87A**, 237–253, doi:10.2151/jmsj.87A.237.

——, K. Gepalan, and R. F. Ferraro, 2011: Developing winter precipitation algorithm over land from satellite observations and C3VP field campaign. *2011 PMM Science Team Meeting*, Denver, CO, NASA. [Available online at https://pmm.nasa.gov/meetings/all/2011-pmm-science-team-meeting.]

Wang, W., and P. Xie, 2007: A multiplatform-merged (MPM) SST analysis. *J. Climate*, **20**, 1662–1679, doi:10.1175/JCLI4097.1.

Wolff, D. B., D. A. Marks, E. Amitai, D. S. Silberstein, B. L. Fisher, A. Tokay, J. Wang, and J. L. Pippitt, 2005: Ground validation for the Tropical Rainfall Measuring Mission (TRMM). *J. Atmos. Oceanic Technol.*, **22**, 365–380, doi:10.1175/JTECH1700.1.

Wu, H., R. F. Adler, Y. Hong, Y. Tian, and F. Policelli, 2012: Evaluation of global flood detection using satellite-based

rainfall and a hydrologic model. *J. Hydrometeor*, **13**, 1268–1284, doi:10.1175/JHM-D-11-087.1.

Xie, P., and P. A. Arkin, 1995: An intercomparison of gauge observations and satellite estimates of monthly precipitation. *J. Appl. Meteor.*, **34**, 1143–1160, doi:10.1175/1520-0450(1995)034<1143:AIOGOA>2.0.CO;2.

——, and ——, 1997: Global precipitation: A 17-year monthly analyses based on gauge observations, satellite estimates, and numerical model outputs. *Bull. Amer. Meteor. Soc.*, **78**, 2539–2558, doi:10.1175/1520-0477(1997)078<2539:GPAYMA>2.0.CO;2.

——, and A.-Y. Xiong, 2011: A conceptual model for constructing high-resolution gauge–satellite merged precipitation analyses. *J. Geophys. Res.*, **116**, D21106, doi:10.1029/2011JD016118.

——, and R. Joyce, 2014: Integrating information from satellite observations and numerical models for improved global precipitation analyses. *Remote Sensing of the Terrestrial Water Cycle*, *Geophys. Monogr.*, Vol. 206, Amer. Geophys. Union, 43–59.

——, J. E. Janowiak, P. A. Arkin, R. Adler, A. Gruber, R. Ferraro, G. J. Huffman, and S. Curtis, 2003: GPCP pentad precipitation analyses: An experimental data set based on gauge observations and satellite estimates. *J. Climate*, **16**, 2197–2214, doi:10.1175/2769.1.

——, M. Chen, A. Yatagai, T. Hayasaka, Y. Fukushima, and S. Yang, 2007: A gauge-based analysis of daily precipitation over East Asia. *J. Hydrometeor.*, **8**, 607–626, doi:10.1175/JHM583.1.

——, ——, and W. Shi, 2010: CPC Unified gauge-based analysis of global daily precipitation. *24th Conf. on Hydrology*, Atlanta, GA, Amer. Meteor. Soc., 2.3A. [Available online at https://ams.confex.com/ams/90annual/webprogram/Paper163676.html.]

——, S.-H. Yoo, W. Wang, A. Kumar, L. Zhang, and W. Ebisuzaki, 2012: Seasonal, interannual, intraseasonal and diurnal variations of global precipitation depicted in the reanalyses and observations. *4th Int. Conf. on Reanalysis*, Silver Spring, MD, WCRP, UA-50. [Available online at https://www.wcrp-climate.org/ICR4/posters/Xie_Seasonal_Interannual.pdf.]

——, and Coauthors, 2014: An in situ-satellite blended analysis of global sea surface salinity. *J. Geophys. Res. Oceans*, **119**, 6140–6160, doi:10.1002/2014JC010046.

——, R. Joyce, and S. Wu, 2016: Recent progress on the second generation CMORPH. *2016 PMM Science Team Meeting*, Houston, TX, NASA. [Available online at https://pmm.nasa.gov/meetings/all/2016-pmm-science-team-meeting.]

Xu, B., S.-H. Yoo, and P. Xie, 2010: Quantifying error in the CMORPH satellite precipitation estimates. *2010 Fall Meeting*, San Francisco, CA, Amer. Geophys. Union, Abstract H14A-06.

——, P. Xie, M. Xu, L. Jiang, C. Shi, and R. You, 2015: A validation of passive microwave rain-rate retrievals from the Chinese *FengYun-3B* satellite. *J. Hydrometeor.*, **16**, 1886–1905, doi:10.1175/JHM-D-14-0143.1.

Yong, B., Y. Hong, L.-L. Ren, J. J. Gourley, G. J. Huffman, X. Chen, W. Wang, and S. I. Khan, 2012: Assessment of evolving TRMM-based multisatellite real-time precipitation estimation methods and their impacts on hydrologic prediction in a high latitude basin. *J. Geophys. Res.*, **117**, D09108, doi:10.1029/2011JD017069.